MICROSEISMIC REFLECTION IMAGING

DISSERTATION

zur Erlangung des Grades eines

DOKTORS DER NATURWISSENSCHAFTEN

am Fachbereich Geowissenschaften
der Freien Universität Berlin

vorgelegt von

Anton Reshetnikov

Berlin
September 2013

Ich erkläre hiermit an Eides statt, dass ich die vorliegende Dissertation selbstständig und nur unter Verwendung der angegebenen Quellen und Hilfsmittel angefertigt habe.

Berlin, 6. September 2013

Summary

The aim of this work is to expand the list of possible applications of microseismic data and use it for reflection imaging. Microseismic events are considered as an analogue of active seismic sources and the corresponding wavefield is treated as seismic reflection data. In this thesis a special method is developed that takes the specific character of microseismic waveforms into account and allows its use this wavefield for the imaging of seismically active zones.

The first question one has to answer is whether any reflected waves are presented in the microseismic recordings. To check this, a new algorithm for grouping and sorting seismograms is proposed. The produced seismic data gathers show that in many cases microseismic waveforms contain coherent signals that can be associated with reflections. Low energy and the complicated radiation patterns of microseismic sources as well as the usually restricted data aperture, make the application of conventional imaging techniques problematic. The Microseismic Reflection Imaging method employs the directional migration approach called "Fresnel Volume Migration". It strongly reduces the imaging artefacts caused by the low aperture of the data, but it requires the estimation of the polarity of the wavefield. Unfortunately, the exact calculation of the polarisation is not always possible for weak microseismic signals. The proposed method uses a hodogram analysis to identify the parts of the recordings for which one can get a reliable polarisation. Only these parts are then used for imaging, while the rest of the data are automatically excluded. The method takes advantage of the unique properties of microseismic data, such as location of the microseismic sources directly inside the area of interest and the high frequency of reflection data. This allows one to get images of small-scale heterogeneities in a seismically active zone or stimulated reservoir.

The Microseismic Reflection Method is applied to both natural and induced seismicity data sets with various data qualities and acquisition geometries. The first considered dataset is natural seismicity data acquired at the San Andreas Observatory at Depth (SAFOD). There are six events recorded by an 80 receiver array installed in the monitoring well. The obtained result reveal a distinct image of the fault branch nearby the borehole. This result is in good agreement with the available borehole lithology information as well as with the existing active seismic reflection images.

The method is also applied to the induced seismicity data from the German Continental Deep Drilling Programme (KTB). The dataset includes seismograms from 50 weak events recorded at the single borehole receiver. The corresponding image covers only a small volume in the vicinity of the microseismic cloud. However, the revealed reflector is in agreement with the large-scale fault zone image obtained by active seismic profiling.

The third considered dataset is the induced microseismic data acquired during the stimulation of the enhanced geothermal system in Basel, Switzerland. This dataset includes more than 2000 events recorded at six borehole sensors. The reflection images reveal the distinct network of reflectors in the vicinity of the injection point, inside the microseismic cloud. These reflectors correlate well with the available borehole ultrasonic imager data. The detailed high-resolution images of the Basel EGS reservoir together with the spatial distribution of the events and their fault plane solutions are analysed and a possible interpretation is presented.

The application results show the potential of microseismic waveform data for seismic reflection imaging. Migrated microseismic reflection data can provide information about the internal structure of a seismically active zone or a stimulated reservoir. Moreover, the presented method helps to observe the features of a seismically active area that are not visible to other methods.

Zusammenfassung

Das Ziel dieser Arbeit ist es das Repertoire der Anwendungsmöglichkeiten mikroseismischer Daten zu erweitern und für die reflexionsseismische Abbildung zu nutzen. Hierbei werden mikroseismische Ereignisse als Äquivalent zu aktiven seismischen Quellen behandelt sowie die korrespondierenden Wellenfelder als seismische Reflexionen. In dieser Arbeit wird eine neue Methodik entwickelt, welche die spezifischen Charakteristika mikroseismischer Wellenfelder berücksichtigt und geeignet ist, seismisch aktive Zonen abzubilden.

In einem ersten Schritt muss geklärt werden, ob und inwiefern reflektierte Wellen in mikroseismischen Datensätzen auftreten. Hierzu wird ein Algorithmus zur Gruppierung und Sortierung der Seismogramme vorgestellt. Die erstellten Seismogrammsektionen (*Seismic Data Gathers*) zeigen, dass in vielen Fällen die mikroseismischen Aufzeichnungen kohärente Signale enthalten, welche mit Reflexionen assoziiert werden können. In vielen Fällen beeinträchtigen die geringe Energie, das komplizierte Abstrahlungsmuster und die kleine Apertur mikroseismischer Quellen die Anwendbarkeit konventioneller Abbildungsverfahren beträchtlich. Die hier entworfene *Microseismic Reflection Imaging* Methode basiert auf der Fresnel Volumen Migration (FVM), welche die Richtungsinformationen der aufgezeichneten Wellenfelder berücksichtigt. Die FVM verringert Abbildungsartefakte, welche durch eine geringe Apertur entstehen, erfordert jedoch die Abschätzung der Wellenfeldpolarisation. Diese ist für schwache mikroseismische Daten allerdings nicht immer durchführbar. Das hier vorgeschlagene Verfahren bemüht die Hodogrammanalyse zur Identifizierung jener Zeitfenster innerhalb der Seismogramme, welche eine verlässliche Bestimmung der Polarisation erlauben. Ausschließlich diese Abschnitte werden im Folgenden verwandt, die anderen Teile werden automatisch aussortiert. Das Verfahren nutzt Vorteile mikroseismischer Daten, wie die Anwesenheit seismischer

Quellen im Zielvolumen und die hohe Frequenz der Reflexionen gezielt aus. Somit können auch kleine Heterogenitäten innerhalb seismisch aktiver Zonen bzw. stimulierter Reservoire abgebildet werden.

Die mikroseismische Reflexionsmethode wird an Datensätzen natürlicher und induzierter Seismizität getestet, wobei sich Datenqualität und Stationsverteilung stark voneinander unterscheiden. Der erste Datensatz beruht auf natürlicher Seismizität und stammt vom San Andreas Observatory at Depth (SAFOD). Hierbei wurden sechs Ereignisse durch 80 Stationen eines Bohrlocharrays aufgezeichnet. Die Auswertung ergibt ein klares Bild des Störungssystems nahe des Bohrlochs, welches ein Ergebnis von guter Übereinstimmung mit der vorhandenen Lithologieinformation eines nahen Bohrlochs sowie mit anderen unabhängigen aktiven reflexionsseismischen Messungen darstellt.

Für eine zweite Anwendung werden Daten des deutschen Kontinentalen Tiefenbohrprogramms (KTB) genutzt. Hierbei wurden 50 schwache Ereignisse durch eine einzelne Bohrlochsonde aufgezeichnet. Das entsprechende Abbild des Untergrundes deckt zwar nur einen kleinen Teil des Volumens in der Nähe der seismischen Wolke ab, allerdings stimmen die abgebildeten Reflektoren mit dem gröber aufgelösten Abbild der Verwerfungszone überein, welche aus einem aktiven seismischen Profil bestimmt wurde.

Der dritte Datensatz stammt aus der Stimulationsphase des Basel EGS (Enhanced Geothermal System) in der Schweiz. Hierin sind über 2000 Ereignisse enthalten, welche von sechs Bohrlochseismometern aufgezeichnet wurden. Die Anwendung der hier neu entwickelten Methode ergibt ein klares Bild eines ausgeprägten Netzwerkes von Reflektoren in unmittelbarer Nähe zum Injektionspunkt, innerhalb der seismischen Wolke. Daten eines Ultraschalllogs bestätigen die Lage dieser Reflektoren. Das detaillierte, hochauflösende reflexionsseismische Abbild wird zusammen mit der räumlichen Verteilung der Ereignisse sowie über Herdflächenlösungen analysiert und interpretiert.

Die Ergebnisse dieser drei Anwendungen belegen das Potential mikroseismische Daten für reflexionsseismische Abbildungsverfahren zu nutzen. Aus migrierten reflexionsseismischen Daten lassen sich Informationen über die aktive seismische Zone bzw. das stimulierte Reservoir gewinnen. Insbesondere stellt die hier entwickelte Methode eine Möglichkeit dar auch kleinska-

lige Reservoireigenschaften zu finden und abzubilden, welche von anderen Abbildungsverfahren nicht gesehen werden können.

x

Acknowledgements

I feel tremendously lucky to have the opportunity to work with my supervisor Prof. Dr. Serge A. Shapiro and would like to thank him for his guidance and support during all the years at Freie Universität Berlin. I greatly appreciate all the numerous and fruitful discussions we have had. I am very thankful to Prof. Dr. Stefan Buske, my second supervisor, who helped me to start this project and provided me with valuable advice and instructions as well as some of his software. This has extremely facilitated my work at the initial stage.

Besides my supervisors, I would like to thank the rest of my thesis committee: Prof. Dr. Frederik Tilmann, Prof. Dr. Mark Handy and Dr. Carsten Dinske for their time and consideration.

I would like to thank Dr. Jörn Kummerow who was always generous with sharing his time and experience. Our discussions significantly contributed to this work and I was happy to learn a lot from our collaboration. I would like to acknowledge a great help of Dr. Carsten Dinske who read this thesis and helped me to substantially improve it.

My further thanks goes to Stine Gutjahr for helpful discussions and Andrei Rusu for his help with the data processing and analysis. Special thanks to Jonas Folesky and Antonia Oelke for helping me with translating the abstract of this thesis.

I would also like to thank Nicolas Hummel who has been a very good friend to me both in and out of the institute.

Finally, I would like to thank my friend Anna Nazarova. This work would not be possible without her encouragement and support.

CONTENTS

INTRODUCTION

Over the past decade phenomenon of microseismicity has received increasing attention from both academia and industry (Figure 1.1[1]). There are several areas for which microseismicity is of great interest. The first is in the exploration and development of unconventional oil and gas reservoirs[2]. The demand for oil and natural gas is continuously growing and is expected to grow at least in the next 20 years [Holditch, 2003]. Meanwhile, the peak in production from conventional reservoirs is predicted to occur sometime between 2007 and 2019 [MacKenzie, 1998]. In this situation, the role of reservoirs that demand massive stimulation to be productive increases and will continue to grow in the short-term. Large reservoir stimulation treatments often lead to the production of numerous microearthquakes in the vicinity of the treatment area [Shapiro *et al.*, 2003]. Another example is CO_2 sequestration. Carbon dioxide removal and storage is a technology for reducing the emission of industrial CO_2 into the atmosphere [Damen *et al.*, 2003]. The injection of CO_2 into a fractured reservoir may cause geological instability and even earth tremors [Over *et al.*, 1999]. The problems of global warming and resource depletion are bringing more attention to possible alternative energy sources. One of them is deep geothermal energy. The creation of an enhanced geothermal system includes drilling a hole into a hard non-porous rock and the injection of large amounts of fluid under high pressure in order to make this rock permeable (e.g. Majer *et al.* [2007]). Such stimulation creates microearthquakes that might be felt at the surface or even produce damage [Giardini, 2009].

---

[1]The number of publications includes publications in journals and extended abstract for the conferences published by SEG and EAGE. Obviously the total number of publication related to microseismicity is much larger. Nevertheless the plot clearly shows the general tendency.

[2]Unconventional reservoirs–reservoirs that can be produced at economic flow rates and that produce economic volumes of oil and gas only with large stimulation treatments or with a special recovery process [Holditch, 2003].
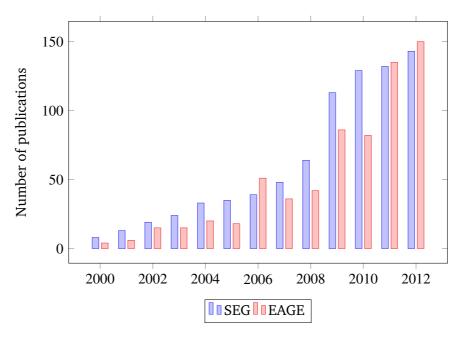
Figure 1.1: The number of publications containing the word "microseismic" in the title, abstract or keyword list published by SEG and EAGE, two major professional organisations of applied geophysicists.

Microseismic data has become a unique tool for the characterisation of different types of reservoirs or tectonic structures. There is a great variety of possible applications available. Induced microseismic event locations are used to monitor the spatial characteristics of newly created or activated fractures (e.g. Rutledge *et al.* [2004]; Maxwell *et al.* [2010]) and evaluate the stimulation volume in the case of hydraulic fracturing or geothermal reservoir development [Mayerhofer *et al.*, 2008]. It is a key tool in estimating the hydraulic transport properties of the rock [Shapiro *et al.*, 1997, 1999, 2002] and the statistical properties of pre-existing fractures [Rothert & Shapiro, 2007]. Microseismic data is also used for the monitoring of geomechanical processes in the rocks (e.g. Teanby *et al.* [2004]). Natural seismicity is spatially related to large-scale faults and can provide useful information about the geometry of large-scale geological structures (e.g. Daneshfar & Benn [2002]; Muñoz *et al.* [2002]; Courboulex *et al.* [2003]).

Potentially, there is an alternative way to use microseismic data. One might think of microseismic events as sources for reflection imaging. Reflection seismic imaging is a well elaborated and widely used approach in the active seismic (e.g. Scales [1995], Schleicher *et al.* [2007]). However, although there have been some attempts to apply

the existing imaging methods to microseismic data directly [Chavarria *et al.*, 2003; Dyer *et al.*, 2008], the results remain somewhat questionable. There is also a technique dedicated to the reflection imaging using microseismic sources namely the Acoustic Emission reflection method [Soma *et al.*, 1997]. It has been shown that this method can be helpful in resolving large heterogeneities near the microseismic cloud. Authors presented images of the geothermal field where the reflectivity below the seismically active zone elongates into solid linear reflectors. However, the same authors have reported that the method was not efficient for imaging structures close to the sources [Soma *et al.*, 2007]. This implies that the method is not able to resolve the most interesting and relevant part – the internal structure of a seismically active zone (the stimulated volume in the case of induced seismicity and the fault zone in the case of natural seismicity). These approaches have been applied to a few datasets and are not in fact widely used. In general, the idea of using microseismic events as sources for reflection imaging has not received much attention.

The purpose of this thesis is to present a new method for microseismic reflection imaging which takes into account the unique features of microseismic data. The main target of the method is the inner part of a seismically active zone. The method includes the complete workflow from the initial input data analysis and selection, and all the necessary interim computations to the final stacking of the output image. In order to demonstrate its potential, the Microseismic Reflection Imaging approach is applied to both natural and induced seismicity datasets with different acquisition geometries.

Chapter 2 provides an overview of previous studies and formulates a list of questions that have not yet been answered. Next, it presents the key principles of the proposed method and shows its complete workflow.

Chapter 3 focuses on the application of the Microseismic Reflection Imaging approach to the natural seismicity data. The chapter considers several natural microseismic events recorded by a borehole array near the San Andreas Fault in California, United States. The obtained results are high-resolution 3D images of different SE-NW oriented reflectors related to the SAF system in the close vicinity of the borehole. To support the findings, it is compared to other active and passive seismic images and the correlation with borehole lithology is analysed. It revealed a predominantly satisfactory agreement for both juxtapositions. Furthermore, the stacked image of several microearthquakes provides a spatial characterisation of the complex internal structure of the SAF, with

much higher resolution than can be obtained from surface seismic reflection data.

Chapter 4 analyses induced microseismic data and shows how the method works in the case of extremely restricted acquisition and a small amount of weak events. The method is applied to the data obtained from the German Continental Deep Drilling programme (KTB project), recorded at a single borehole sensor. The image is constructed using data from 58 microseismic events. There are several distinct reflectors revealed within the microseismicity cloud that belong to a large fault zone. In order to check the consistency of the obtained results, they are compared to seismic attributes obtained from the surface seismic 3-D depth migrated image. The result is mostly consistent with seismic attributes by location and dip.

Chapter 5 presents the results of the microseismic reflection imaging applied to the induced seismicity data from the stimulation of the Enhanced Geothermal System at Basel, Switzerland. The dataset contains more than 2000 events recorded at six shallow and downhole borehole sensors providing good spatial coverage. Moreover, the seismic data quality is much better than the data considered in the previous chapter. Compared to other examples of applications, this chapter conducts a much more detailed analysis and shows more substantial results. It presents P- and S-wave reflection images for the data recorded at four different sensors. The obtained images reveal the consistent high resolution reflector network in the vicinity of the injection, inside the microseismic cloud. In order to illustrate the limitations of the method, it is demonstrated how the image quality degrades with increasing distance between the stimulated volume and the receiver. The results are compared with the injection borehole ultrasonic image as well as the V_P/V_S ratio distribution revealing a quite good agreement. At the end, a joint interpretation of the obtained images and the event locations is provided.

Chapter 6 summarises the findings of this work. It discusses possible applications of the method and its limitations. Finally, further directions of future work are discussed.

METHODOLOGY

The focus of this work is to elaborate a method that would allow the imaging of microseismic reflection data considering microseismic events as active seismic sources. The target of imaging is a seismically active zone or a stimulated volume for the case of induced seismicity. Reflection-seismic imaging is a well established approach widely applied in exploration seismology since 1930s [Bednar, 2005]. There are many migration algorithms based on different physical approximations and applicable to different types of seismic data. Nevertheless, microseismic data have a set of unique features that distinguish it from any other active seismic data. These features have to be taken into account in order to get a reasonable result for the given problem.

Particularly, in contrast to active seismic, microseismic events are not controlled sources, though their location in the case of proper acquisition can be determined. Moreover, the area of interest is likely to be the same seismically active zone where microseismicity occurs. This means that microseismic sources are located in the direct vicinity of a target and at a distance from seismic sensors in contrast to surface, VSP and marine data where sources are at a distance from a target.

Acquisition geometries used for microseismic monitoring are different from geometries of land seismic or VSP. Since the main purpose of microseismic monitoring is to detect the arrival times of events, the number of receivers in microseismic acquisition systems is usually much smaller and they are sparsely distributed. Among other limitations, this restricts applicability of any post-stack imaging. In some cases, amount of events can reach hundreds or even thousands, which is usually one or two orders of magnitude larger than the number of sensors.

The sources used in active seismic are different kinds of explosions, vibrators or air guns with well known and in most cases spherical radiation patterns. On the other hand, microseismic events are small earthquakes with complicated focal mechanisms, which might be initially unknown. These focal mechanisms as well as source energies can vary significantly even for events located close to each other. Furthermore, microseismic sources have higher frequency and lower energy signals compared to conventional seismic sources.

In this chapter I will present the methodology and complete workflow for the microseismic reflection imaging approach that addresses the complications introduced by microseismic sources. This method will then be applied to both natural and induced seismicity data in the following chapters.

2.1 Previous studies

The use of microearthquakes as seismic sources is not a well established technique. Although there are some studies published on this topic. To my knowledge, the first attempt to use reflected waves in an earthquake seismogram to characterise a subsurface was performed by Sanford *et al.* [1973]. Authors analysed microearthquake seismic data recorded by sensors located near Rio Grande rift, New Mexico. Having event locations, they identified SP and SS reflected phases and mapped a sharp dipping discontinuity at a depth of 18 to 30 km. The mapping process did not involve any sophisticated migration procedure and was based on the reflected wave travel time analysis. Nevertheless, authors have demonstrated the presence of the reflected waves in microseismic coda, and, therefore, a possibility to image microseismic reflection data.

Acoustic Emission reflection method

Soma & Niitsuma [1997] and Soma *et al.* [1997] firstly proposed the technique dedicated to imaging reflections in microseismic data. The technique was called Acoustic Emission (AE) reflection method. To identify reflected phases they used analysis of the 3D hodogram in the time domain. More precisely they computed global polarisation coefficient [Samson, 1977] as a function of time for each 3-component seismogram

from a microseismic event. Authors assumed that time periods of coherent wave arrivals such as direct or reflected waves were highly linear in contrast to a non-linear incoherent random noise. To find the position of a reflector they performed diffraction stack migration, but instead of stacking reflected wave amplitudes or energies, they stacked polarisation coefficient (further denoted as linearity) values. These values were stacked on the iso-delay ellipsoid corresponding to the reflected wave travel time[1].

In order to improve resolution, the authors estimated polarisation of the S-wave as a vector corresponding to the largest eigenvalue of the covariance matrix computed from the three component seismogram. Possible wave propagation directions were limited to a plane perpendicular to this vector. Consequently, the ellipsoid of all possible reflection points for a given time was restricted by the intersection with this plane i.e. to a narrow band on the ellipsoid. Final image was obtained by stacking the linearity over corresponding bands for all possible time delays and for all microseismic events.

Soma *et al.* [2002a] further updated the AE reflection method by considering the covariance matrix in the time-frequency domain. To get the image in the extended version of AE reflection method linearity values were stacked over all possible time delays and frequency bands. It was done to detect more reflectors and improve the resolution of the final image.

Later Tamakawa *et al.* [2010] and Asanuma *et al.* [2011b] proposed to use microseismic multiplets as sources for AE reflection method to improve imaging accuracy by using additional information about relative times between multiple events.

AE reflection method was applied to the data from several geothermal projects such as Kokkonda geothermal field [Soma & Niitsuma, 1997] and Soultz Hot Dry Rock experiment [Soma *et al.*, 1997, 2002a, 2007]. The most comprehensive results are presented in Soma *et al.* [2007] where the authors integrated reflection images obtained by the AE reflection method using the Soultz data from 1993 to 2003.

There are several issues that limit the applicability of the AE reflection method:

- AE reflection method assumes a homogeneous and isotropic velocity model. This

---

[1]Iso-delay ellipsoid – the distribution of virtual reflection points for a given travel time of a reflected wave which is determined by the location of the detector and the source [Soma *et al.*, 1997].

allows to explicitly estimate the distribution of possible reflection points for each time delay, which is in this case ellipsoid with the focus points at a source and receiver. In the general case and especially for the situation of a distributed acquisition system, the accuracy of such approach is questionable.

- All the reflection data imaged by the AE reflection method assumed to be reflected S-waves. It is explained by much stronger energy of S-waves that dominates in the observations and can cover the reflected P-waves (e.g. Soma *et al.* [2002b]). In fact, PP reflections in some cases can be observed in a coda between direct P- and S-waves, which will be shown in the following chapters. Moreover, the authors do not estimate the direction of wave propagation for detected reflected waves. They estimate polarisation vector of S reflections to limit possible directions of wave propagation to a plane perpendicular to this vector. It allows to restrict distribution of possible reflection points to a band on iso-delay ellipsoid, which indeed improves the image. Nevertheless, even restricted stacking introduces significant ambiguity to the final image. Such ambiguity can only be reduced by stacking wide aperture data, but for microseismic acquisition systems data aperture is usually restricted. Effectively this procedure is on a half way from the standard pre-stack Kirchhoff depth migration where amplitudes are stacked on a complete surface formed by potential reflection points for a given reflected wave travel time and the Fresnel-Volume-Migration [Lüth *et al.*, 2005; Buske *et al.*, 2009] where stacking is limited to the region around potential reflection point.

- A serious drawback of the AE reflection method comes from two assumptions. First, the high linearity at all frequencies directly indicates the presence of P– or S-wave. Second, the polarity estimates are equally correct for all highly linear parts of a seismogram at different frequencies. While reflected waves in a 3-component seismogram indeed expected to be highly linear, this assumption does not take into account quite probable presence of artificial or natural polarised noise. There are frequency bands in which coherent noise and useful signal are strong. Also, most likely these bands overlap. Thus, even for highly linear signals, corresponding polarity estimates are not equally correct for different parts of the frequency spectrum. This leads to potential misinterpretation of the coda and inaccurate polarity estimates in the case of correctly detected reflected wave at frequencies where the artificial noise is strong enough.

It has been shown that AE reflection method can resolve large heterogeneities nearby

the microseismic cloud. The authors showed images of the geothermal field where reflectivity below the seismically active zone elongates into the solid linear reflectors. On the other hand, in the vicinity of microseismic sources reflectors appeared to be piecewise spots of reflectivity that do not form any linear structures. The authors reported that the method was not efficient for imaging structures close to the sources [Soma *et al.*, 2007].

Conventional imaging techniques

There are also several studies that attempt to apply conventional imaging techniques to the microseismic reflection data without any adaptation. For instance, Chavarria *et al.* [2003] presented their results of imaging the reflection data from the natural microearthquakes recorded at SAFOD pilot borehole. Similarly, Dyer *et al.* [2008] showed images of potential fractures by migration of the induced microseismic data in the area around the Upper Rhine Graben near Basel. The authors use Kirchhoff pre-stack depth migration algorithm. Though both results revealed highly reflective parts of the area around the microseismic sources, it is hard to interpret the obtained images because of strong migration artifacts caused by low spatial coverage of microseismic data.

2.2 Problem formulation

Previous studies have shown that microseismic reflection data can potentially be migrated and can image large-scale geological structures nearby microseismic sources. Though, it was problematic to resolve the internal structure of a seismically active zone.

There is also a number of questions that have not yet been answered:

- How to check if there are reflections in microseismic data?

- How to evaluate the quality of microseismic reflection data and check if it is possible to use it for imaging?

- How to define a target for microseismic reflection imaging?

- How to process and migrate microseismic reflection data in a way that minimises migration artifacts and provides result independent of observation conditions?

The purpose of this chapter is to cover these questions and to present complete workflow for processing and imaging microseismic reflection data.

2.3   The concept of Microseismic Reflection Imaging

In order to solve the problem of microseismic reflection imaging, one has to take into account peculiarities of microseismic data and acquisition systems. The data quality within one dataset can be rather versatile, due to diversity of microseismic source energies and radiation patterns. Thus, not all the events are suitable for imaging, so the first step has to be the data analysis and exclusion of events that have large location errors or unacceptably low signal to noise ratio.

The main problem impeding application of conventional imaging techniques is the mutual disposition of sources and receivers. Particularly, it is a very narrow aperture of the data. In order to handle it, in addition to amplitudes of seismograms, it is necessary to consider the direction of wave propagation of reflected waves and then employ migration algorithm that uses this information in order to reduce artefacts in the final image. Since estimation of direction of wave propagation is essential for microseismic reflection imaging, it is important to take into account factors influencing the accuracy of this estimates. One of these factors is ambient noise, which usually has a non-uniform frequency spectrum. This implies that recorded useful signal as well as noise are stronger or weaker at some frequency bands. In order to improve the accuracy of directivity estimates one has to find frequency band at which signal is stronger than noise.

Considering low energies of microseismic sources it is also important to exclude parts of seismograms that are not providing any stable polarity estimates. To do this one needs to introduce quality factors for estimated direction of wave propagation as functions of time. Then one can specify thresholds for this factors to distinguish between reliable and unreliable parts of the data. It is also problematic to separate different types of reflected waves. Potentially it can introduce ghost reflectors in the image. For example reflected S-wave migrated as PP reflection would be imaged at completely

wrong place because of different velocity and direction of wave propagation. In order to reduce the contribution of misinterpreted waves one can restrict the imaging volume to a seismically active area. Reduction of the imaging volume does not guarantee that misinterpreted waves would not contribute to the image, but it would weaken this effect.

The principles of Microseismic Reflection Imaging can be formulated as follows:

- use only microseismic events with relatively small location misfits and high enough signal to noise ratio;

- use a directional migration approach to solve the problem of limited aperture;

- determine the frequency range for which the signal provides the most accurate estimates of the polarisation;

- use only those parts of seismogram for which one can estimate accurate polarisation information;

- use restricted imaging volumes in order to reduce the contribution of misinterpreted waves to the final image.

2.4   Event selection and arrangement

To estimate polarity of a reflected wave, it is required that the corresponding wavelet is above the noise level. While in order to locate an event, one only has to detect the arrival times of the direct P- and S-waves.[1] This makes the imaging problem much more sensitive to the quality of seismic data than the problem of microseismic event location. Therefore, not all locatable events are suitable to be used as sources for the reflection imaging. To sort out unusable events one can use two criteria: location error and signal to noise ratio (can be determined using direct wave arrival time picks). Using pre-defined thresholds for acceptable RMS error and signal to noise ratio one can select a subset of events, which can then be used for imaging. In the case of distributed acquisition systems of multiple monitoring wells, signal to noise ratio can

---

[1]Here I consider microseismic data recorded at downhole sensors and travel time grid search based location algorithms.

vary for different sensors. Therefore, it makes sense to process the data recorded at different receivers individually and to produce different subsets of suitable events for each receiver or array of receivers.

To facilitate further data analysis and processing, selected traces can be grouped into common-receiver gathers. The final image is obtained by stacking of images of individual traces; therefore, the order of the traces in a gather does not play any role. However, for the sake of visual assessment and interpretation of the data it makes sense to arrange traces in a way, that makes it easy to identify possible coherent reflections within a gather. I propose the following algorithm: first, all traces are shifted in a way that their time zero coincides with the corresponding event triggering time. Then the first trace is taken for the event at the edge of the cloud of events selected for a given receiver. Each next trace is taken for the event that is the closest one to the event corresponding to the previous trace in a gather (see Figure 2.1). This algorithm allows to sort seismograms in a way that neighbour traces in most cases correspond to events located close to each other. Although it is possible that at the end of a gather there will be several traces corresponding to events at relatively large distances from each other.

Part of a common receiver gather produced from induced microseismic events is shown in Figure 2.2. Through the use of the sorting algorithm neighbour traces in a gather have similar travel times and coda. This allows to evaluate the quality of the time picks and computed event origin times. Even more importantly, it helps to identify potential reflections within the data.

2.5 Polarisation estimation

In most cases, the spatial dimensions of a microseismic cloud are small or comparable to the distances from events to a monitoring system. Accordingly, the aperture of scattered waves for such system is low in comparison to wide-angle active seismic data. In this situation, the only way to get a resolved image of the cloud interior is to take into account polarity of the reflected waves.

To obtain a wave propagation direction of a 3-component seismic trace, we use auto- and cross-variances of time samples within a time window that have to include several dominant periods of P- or S-wave [Jurkevics, 1988]
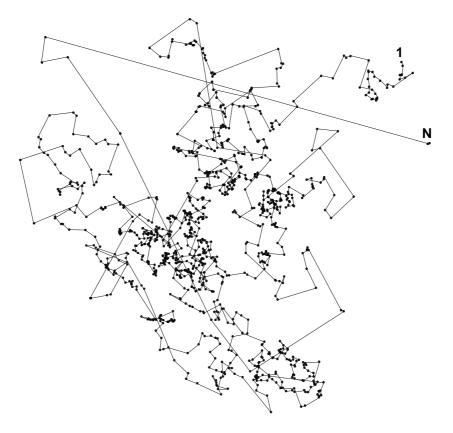
Figure 2.1: Sequence of events in a common receiver gather starting from the first event (1) to the last one (N).

$$C_{ij} = \frac{1}{N} \sum_{n=T-\frac{1}{2}N}^{T+\frac{1}{2}N} u_i(n)u_j(n) \qquad i, j = \{1, 2, 3\}$$

where i and j are seismic trace component indexes, $u_i(n)$ is the n-th sample value of i-th component of a trace, T is a time sample number for which direction is being estimated, N is a time window length. By solving the eigenvalue problem

$$(C - \lambda I)p = 0 \qquad \lambda_1 \leq \lambda_2 \leq \lambda_3$$

one can get corresponding eigenvectors and eigenvalues. Then, the eigenvector $\vec{p_3}$ corresponding to the largest eigenvalue defines the direction of linear component of
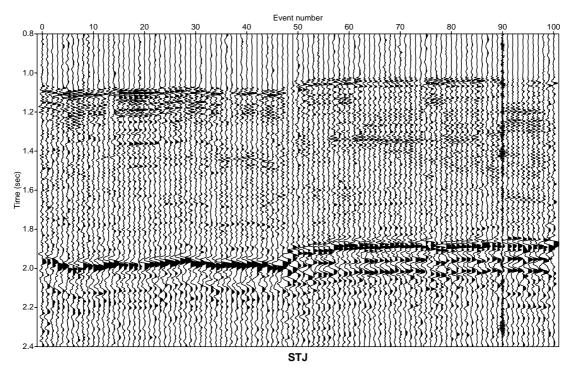
Figure 2.2: Common receiver gather produced from induced microseismic events.

the hodogram and therefore represents P-wave polarisation at the current time. To specify S-wave propagation direction I use eigenvector $\overrightarrow{p_1}$ corresponding to the smallest eigenvalue, which by definition is orthogonal to the particle motion hodogram (see Figure 2.3).

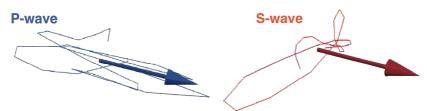Figure 2.3: Hodograms of P- and S-waves for a three component seismic data and corresponding wave propagation directions.

One can also formulate the quality control functions for estimates of wave propagation direction. For P-waves, it is clear that the more linear shape of the hodogram leads to the more accurate estimate of P-wave polarity. Linearity of the hodogram can be defined as follows (adapted from Samson [1977])

$$R = \frac{(\lambda_1 - \lambda_2)^2 + (\lambda_2 - \lambda_3)^2 + (\lambda_3 - \lambda_1)^2}{2(\lambda_1 + \lambda_2 + \lambda_3)^2}.$$

Linearity has small positive values for non-coherent noise and tends to 1 for the case of perfectly linear signal ($\lambda_1 \ll \lambda_3$ and $\lambda_2 \ll \lambda_3$).

I also introduce the quality control function for S-wave propagation direction estimates. Direction of S-wave can be accurately estimated if the hodogram is flat and circular. This condition is satisfied in the case when $\lambda_2 \gg \lambda_1$ (then $\lambda_3 \gg \lambda_1$ by definition). Therefore, "flatness" of the hodogram can be defined as

$$C = \frac{\lambda_2^2 + (\lambda_2 - \lambda_1)^2}{2(\lambda_2 + \lambda_1)^2}.$$

Hodogram "flatness" values vary from $\frac{1}{2}$ that indicates linearly polarized or non-coherent signal and 1 that indicates that the hodogram is flat and circular and hence the orthogonal direction can be estimated accurately.

Values of linearity and "flatness" as a function of time for each seismogram can be then used to identify parts of seismic data for which it is possible to estimate reliable wave propagation direction. Figure 2.4 illustrates this procedure. Only those parts of the seismogram which have linearity values larger than a given threshold (marked with red bars in Figure 2.4) are taken for further imaging. It significantly reduces noise and migration artefacts in the final image.

Analysis of linearity and "flatness" of the 3D hodogram is helpful for detecting consistent signals. The fact that at some time and at some frequency linearity of the hodogram is high likely indicates that there is a coherent signal at this time. However, it does not guarantee that the polarity estimated for this frequency is correct. For example, usually signals are more linear at lower frequencies, but polarities estimated at lower frequencies can be wrong.

In order to get accurate estimates of direction of wave propagation I propose to make an additional processing step. The goal of this procedure is to estimate frequency band that provides the most reliable reflected wave propagation direction estimates. In the general case, there is no a priori information about the position of reflectors and
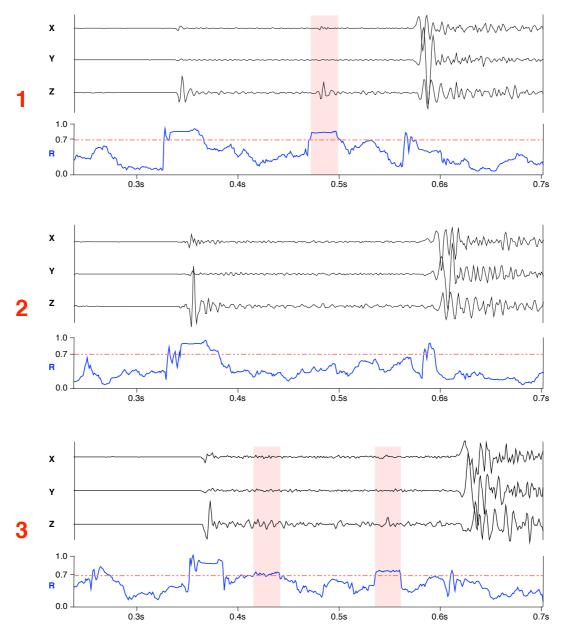
Figure 2.4: Seismograms from three microseismic events and corresponding P-wave linearity values as a function of time.

therefore information about reflected wave incident angles. Though, coordinates of sources and receivers are known and therefore theoretical polarity of the direct waves can be calculated, for example, by tracing rays from microseismic sources to a receiver. Assuming that the frequency bands of direct and reflected waves of the same type are close to each other, one can build an optimisation procedure where variables are

parameters of the filter (see Figure 2.5) and the criterion is the difference between the empirical and theoretical polarity estimates of the direct wave.
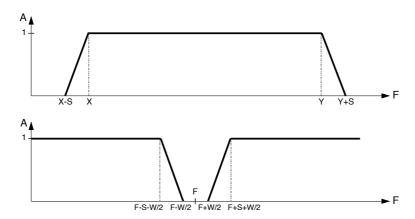

Figure 2.5: Parameters of band-pass and notch frequency filters used for the optimisation.

The complete workflow of wave propagation direction estimation consists of 4 steps:

1. Use optimisation procedure to find a frequency filter that provides the most accurate polarity estimates by minimisation of the misfit between empirical and predicted polarisations of the direct wave. It is done for P- and S-waves independently. The by-product of this optimisation procedure is the sensor azimuthal orientation (in the case when it is unknown).

2. Use obtained angle to rotate seismic data recorded at particular sensor from local XYZ to the geographical ENZ coordinates and apply the frequency filters to get two filtered gathers optimised for P- and S-wave polarity estimation.

3. Use filtered data to estimate direction of wave propagation for each time at each 3-component trace for both wave-types.

4. Use linearity (for P-waves) and hodogram flatness (for S-waves) threshold to exclude parts of traces that have unreliable polarity estimates (see Figure 2.4)

As a result of this workflow for each coherent part of a seismogram one can get two direction estimates: one from the assumption that it is the P-wave and another one from the assumption that it is the S-wave. While, unreliable noisy parts of seismogram are excluded by linearity/flatness analysis.

2.6 Imaging procedure

Precise estimation of the direction of wave propagation is an essential part of Microseismic Reflection Imaging. Besides that, it is also necessary to employ imaging algorithm that would take the advantage of estimated polarities. In this study I use the Fresnel-Volume-Migration method presented in Lüth *et al.* [2005] and Buske *et al.* [2009]. This is an extension of pre-stack Kirchhoff depth migration that takes into account a wavefield polarisation information to restrict the migration operator to a region around the actual reflection point. The motivation for this choice is that this algorithm is targeted to resolve spatial ambiguities caused by limited aperture and low spatial coverage. Moreover it is based on well tested and widely used Kirchhoff pre-stack depth migration.

Principles of Kirchhoff pre-stack depth migration

Kirchhoff migration is based on the integral solution of the wave equation. It uses Green's function theory and can be defined as the diffraction stack integral (see e.g. Schneider [1978]; Schleicher *et al.* [1993]; Biondi [2006])

$$I(\mathbf{r}) = \int_A W(\mathbf{r}, \boldsymbol{\xi}) \, U(\boldsymbol{\xi}, t) \, d\boldsymbol{\xi}, \tag{2.1}$$

where $I(\mathbf{r})$ is the image value at point $\mathbf{r}$, $\boldsymbol{\xi}$ is the vector describing source-receiver pairs (see Schleicher *et al.* [1993] for details), A is the acquisition surface, $W(\mathbf{r}, \boldsymbol{\xi})$ is a weighting function, which is used to take into account geometrical spreading effect in the seismic data in order to compute true-amplitude image and $U(\boldsymbol{\xi}, t)$ is the input reflection data. t is time that the considered wave needs to propagate from the source point $\boldsymbol{\xi_s}$ to the image point $\mathbf{r}$ and back to the receiver point $\boldsymbol{\xi_r}$

$$t(\boldsymbol{\xi}, \mathbf{r}) = t(\boldsymbol{\xi_s}, \mathbf{r}) + t(\mathbf{r}, \boldsymbol{\xi_r}). \tag{2.2}$$

Since in reality seismic data is recorded at a discrete set of receivers, the integral 2.1

can be approximated by a sum [Biondi, 2006]:

$$I(\mathbf{r}) = \sum_{i \in A} W(\mathbf{r}, \boldsymbol{\xi}_i) \, U(\boldsymbol{\xi}_i, t).$$ (2.3)

Effectively the migration process for each source-receiver pair $\boldsymbol{\xi}$ can be described as stacking the input seismic data values $U(\boldsymbol{\xi}, t)$ along certain summation surfaces. For each time t the summation surface or isochrone can be defined as a set of all possible image points $\mathbf{r}$ that satisfy equation 2.2. Kirchhoff pre-stack depth migration process for a single trace in the situation of constant velocity is schematically shown in Figure 2.6.
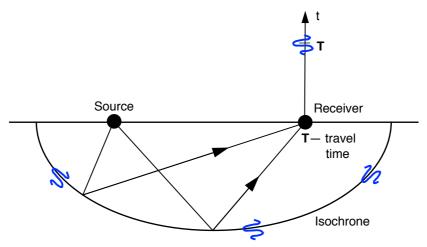

Figure 2.6: Imaging process of a single trace using standard Kirchhoff migration approach.

For large aperture data, when images from many traces recorded at densely located receivers, stacking of images from neighbouring receivers will enhance the image amplitude by constructive interference at areas of actual reflectors and diffractors. On the other hand, for the parts of imaging volume without any reflecting objects stacking will diminish the final image amplitudes. This makes pre-stack Kirchhoff depth migration approach robust and stable for situations of wide angle data.

However, in the situation of restricted aperture and low coverage when reflections illuminate only small parts of reflectors, the standard Kirchhoff imaging approach may produce significant migration noise and artefacts. For this reason Kirchhoff pre-stack depth migration cannot be directly applied to microseismic data.

Fresnel Volume Migration approach

One possibility to reduce migration artefacts in the case of low aperture data is to use polarisation information (see e.g. Takahashi [1995]). For the problem of microseismic reflection imaging, I employ the Fresnel Volume Migration approach proposed by Lüth *et al.* [2005] and Buske *et al.* [2009] that not only uses estimated direction of wave propagation in order to restrict Kirchhoff migration operator to the area around potential reflection point, but also makes reasonable and physically motivated assumption about the size of the reflective area.

According to the Fresnel Volume Migration approach, to migrate a single seismic trace defined by a source-receiver pair $\boldsymbol{\xi}$ for all times t_i one needs to estimate the direction of wave propagation and to trace the ray from the receiver back to the subsurface until it crosses the corresponding Kirchhoff summation surface and finally reaches travel time t_i. Then for each ray one needs to calculate its Fresnel volume [Cervenỳ & Soares, 1992]. Using expression

$$R_F(\mathbf{r}) \approx \sqrt{\frac{T}{\Pi_{13}^{-1}(\mathbf{r}) - (\Pi_{13}(\mathbf{r}) - \Pi_{13}(\mathbf{r_i}))^{-1}}} \tag{2.4}$$

one can estimate Fresnel radius R_F at each point $\mathbf{r}$ on the ray, which is defined by dominant period of the signal T, position of the last point of the ray $\mathbf{r_i}$ at time t_i and element of ray propagator matrix Π_{13} [Ĉervený, 2001; Lüth *et al.*, 2005]. Particularly, one can compute Fresnel radius R_{F_0} at the point where the ray intersects corresponding Kirchhoff summation surface (see Figure 2.7).

Then for each time t on the trace $U(\boldsymbol{\xi}, t)$ the original Kirchhoff migration operator can be restricted to the area inside of the Fresnel volume of the corresponding ray. Mathematically it can be expressed by adding one more factor W_F to the integral 2.1 [Buske *et al.*, 2009]

$$I(\mathbf{r}) = \int_A W(\mathbf{r}, \boldsymbol{\xi}) \, W_F(\mathbf{r}, \boldsymbol{\xi}, t) \, U(\boldsymbol{\xi}, t) \, d\boldsymbol{\xi}, \tag{2.5}$$

where

$$W_F = \begin{cases} 1 & \text{if } d \leq R_{F_0}, \\ 1 - \frac{d - R_{F_0}}{R_{F_0}} & \text{if } R_F < d < 2R_{F_0}, \\ 0 & \text{if } d \geq 2R_{F_0}. \end{cases} \tag{2.6}$$

Weighting factor W_F is designed in a way that it is equal one for all points on the summation surface that have distances to the ray d less than Fresnel radius R_{F_0}. In other words, it has non zero values only for the part of the summation surface that is inside of Fresnel zone of the ray. In order to avoid rough edges in the stacked image weighting factor W_F linearly decay from one to zero with increasing distance from the ray from R_{F_0} to $2R_{F_0}$.
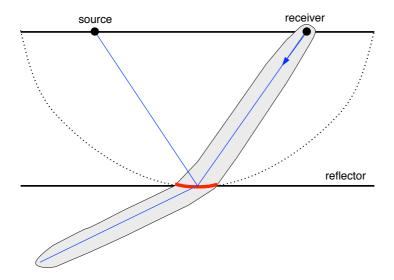

Figure 2.7: Imaging process of Fresnel Volume Migration migration. Dotted line represents Kirchhoff summation surface, blue line is the path of the rays corresponding to the direct and reflected waves, gray area is the Fresnel volume of the ray, red segment is part of summation surface that is inside of the Fresnel volume.

Analogously to Expression 2.3 the Fresnel Volume Migration integral can be written in a discrete form, which is valid for arbitrarily distributed sources and receivers

$$I(\mathbf{r}) = \sum_{i \in A} W(\mathbf{r}, \boldsymbol{\xi}_i) \, W_F(\mathbf{r}, \boldsymbol{\xi}_i, t) \, U(\boldsymbol{\xi}_i, t). \tag{2.7}$$

Moreover, since the radiation patterns of microseismic events may be unknown or in-

accurate, it is problematic to perform true-amplitude microseismic reflection imaging. Therefore in the following I do not consider term $W(\mathbf{r}, \boldsymbol{\xi}_i)$ responsible for true amplitude calculation and instead of 2.7 use simpler expression:

$$I(\mathbf{r}) = \sum_{i \in A} W_F(\mathbf{r}, \boldsymbol{\xi}_i, t)\, U(\boldsymbol{\xi}_i, t). \tag{2.8}$$

Fresnel Volume Migration significantly reduces migration artefacts, especially for low aperture data. Moreover, the fact that function W_F depends on the dominant frequency of the signal makes Fresnel Volume Migration adaptable for diverse microseismic reflection data. Together with the accuracy of wavefield directivity estimates the choice of proper imaging algorithm is of major importance for successful imaging of microseismic reflection data.

Stacking

The input data for the Fresnel Volume Migration procedure is a common receiver gather (see Section 2.4). Each seismogram is migrated separately. The final result is obtained by stacking the images from individual traces. For each trace in a gather I normalise it to the maximal energy in this trace. This is done in order to avoid the situation when the image of the reflection data for one bigger event overpowers and therefore make less visible images for other smaller events.
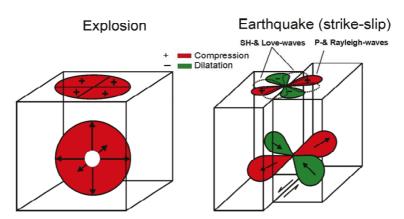

Figure 2.8: Schematic representation of an explosion source and of a strike-slip earthquake along a vertically dipping fault. Figure is taken from Bormann [2002].

Explosion sources used in onshore active seismic have a spherical radiation patterns (see Figure 2.8). This allows to stack amplitudes of seismic data for the imaging. In some cases it is even possible to construct images in terms of true-amplitude values (see e.g. Schleicher *et al.* [1993]).[1] As it shown in Figure 2.8, radiation patterns of microseismic sources are much more complicated. Besides, it is non trivial task to estimate these patterns that has to be done for each event individually and demand a well distributed acquisition system as well as the high signal to noise ratio (see e.g. Hardebeck & Shearer [2002]). In order to stack amplitudes it is necessary to take into account these patterns, otherwise images from two different events illuminating the same reflectors from different angles could weaken the final image by the destructive interference.

In practice, especially in the case of induced seismicity, the fault plane solutions for microseismic events are either unknown or not accurate enough to be included in to the imaging procedure. Therefore in this work I use stacking of absolute values of reflection data amplitudes, which allows to apply the Microseismic Reflection Imaging approach to the data with unknown radiation patterns. Effectively, it decreases the resolution of the final image, but also makes it more stable with respect to small uncertainties of microseismic event location.

In contrast to Soma *et al.* [2007] I do not use any normalisation of the image to the number of events illuminating each point of the subsurface. This is done in order to enhance the areas in the image that are illuminated by many microseismic sources and therefore more likely to be an image if a real heterogeneity inside the reservoir and not a migration artefact. This is especially important in the case of high concentration of microseismic events in a relatively small volume.

2.7   Implementation

A significant part of this work was the implementation of the Microseismic Reflection Imaging approach, which allowed me to process several microseismic datasets and obtain the results presented in the next chapters. Mainly the programming was done by me from scratch using C++ programming language. In some parts of the Fresnel

---

[1]In order to compute true-amplitude images in the case of Kirchhoff migration one need to compute the term $W(\mathbf{r}, \boldsymbol{\xi})$ in 2.1 to take in to account geometrical spreading effect.

Volume Migration code I used Fortran routines provided by Prof. Dr. Stefan Buske to reimplement them on `C++` and adapt to microseismic data. I also used one open source program for travel time computation. Technically the Microseismic Reflection Imaging approach consist of the following software components:

- **Libseis3d** – software library that is used in other programs.

- **SDataPrep** – set of programs performing analysis of input seismic data.

- **MDataPrep** – set of programs preparing the input data for the migration.

- **FDTIMES** – program that performs travel time grid computation.

- **FVMigration** – the implementation of the Fresnel Volume Migration approach.

Libseis3d library contains set of base `C++` objects such as "Velocity Model", "Seismic Data", "Raytracing", providing functionality that is used in other programs. It was developed by me with the exception of part of the raytracing algorithm. I used the Fortran routine provided by Stefan Buske to implement `C++` method performing elementary step on the ray for the raytracing procedure.

SDataPrep software package does initial evaluation and collecting of input microseismic data, analyses location uncertainties and signal-to-noise ratios of microseismic events in order to identify events suitable for further processing. It also performs event sorting as it is described in Section 2.4 and finally produces common receiver gathers. This package has been developed by me completely.

MDataPrep software package is responsible for polarisation analysis of produced common receiver gathers (see Section 2.5). It contains the program that computes direction of wave propagation and identifies parts of seismic data that are suitable for the imaging. There is also a program that performs borehole sensors azimuthal orientation using computed wavefield polarities. This package has been developed by me completely.

FDTIMES – open source software package written by Pascal Podvin (Géophysique / Centre de Géosciences - École des Mines de Paris) that computes travel time grids for smoothed velocity models based on Huygens' principle in the finite difference approximation [Podvin & Lecomte, 1991]. I used it to compute travel time grids for sources and receivers in order to construct isochrones during the migration procedure.

Prof. Dr. Stefan Buske provided me with his Fortran program implementing the Fresnel Volume Migration algorithm, which he used for imaging large surface reflection data profiles. Compared to conventional surface seismic data, microseismic data has much higher frequencies. To take full advantage of such high frequency data, it is necessary to use a much finer migration grid that was not possible with the original Fortran code. For this work, I wrote **FVMigration** program using Stefan Buske's algorithm but implemented it in C++ programming language in order to use **Libseis3d** library and made a number of adaptations and optimisations for microseismic data. Additionally I wrote a version of the **FVMigration** program that is able to perform parallel computations on a multi-node cluster, which is essential for datasets with thousands of microseismic sources.

2.8 Discussion

Microseismic events obviously are not complete analogue of active seismic sources. Consequently, the microseismic reflection imaging cannot be considered as a replacement of the conventional active seismic imaging. There is a number of limitations of the method that come from the nature of microseismic events. Particularly, since such sources are uncontrolled, the illuminated area is also uncontrolled. In contrast to active seismic, state of the art microseismic monitoring systems are focused on reliable event detection rather than providing better subsurface coverage. Therefore, in many cases, for an existing dataset one can get only partial image of a reservoir. Microseismic sources are characterised by low energies that also limits the illuminated volume. In addition to this, the method is demanding to the quality of the data. Strong noise not necessarily implies the impossibility of the imaging, but it strongly reduces amount of usable data. Generally, the noisier seismic traces, the less data to migrate and correspondingly less detailed images are obtained.

Usage of the Fresnel Volume Migration approach helps to reduce migration artefacts caused by low aperture of microseismic data. Nevertheless, stacking is still performed along curved isochrones. This curvature can be weaken by constructive interference of images from neighbouring source-receiver pairs. However, in the case of microseismic data, each part of the imaged subsurface is illuminated by a limited amount of events. For this reason, flat reflector could appear as a slightly curved surface. This

may complicate the interpretation of the resulting image.

Microseismic reflection data has some unique advantages. The most important one is that the sources of imaging are located exactly at the area of interest i.e. stimulated reservoir[1]. Such disposition allows to illuminate parts of a stimulated reservoir that are inaccessible for the surface seismic. Moreover, the resolution of microseismic reflection image can be potentially higher because microseismic sources radiate higher frequency signals.

It is clear that small microseismic sources localised in relatively small area cannot compete with active seismic sources in imaging of large scale structures. However, in the case of proper acquisition, microseismic data potentially can contain high-frequency reflected waves scattered in the local heterogeneities of the reservoir. This means that by applying this specialised imaging technique one can get the image of a reservoir interior with resolution unachievable by conventional surface seismic.

In the following chapters I will present the results of imaging using both natural and induced seismicity under different noise conditions and different acquisition geometries, which demonstrate applicability and potential of the Microseismic Reflection Imaging method.

---

[1]Here I consider seismicity induced by stimulation of a reservoir, but it is also relevant for the case natural seismicity, where seismically active zones are of a great interest.

REFLECTION IMAGING USING NATURAL MICROSEISMICITY

The analysis and interpretation of natural seismicity is receiving an increased attention in academia for the general understanding of seismogenic processes at plate boundaries (e.g Schorlemmer & Wiemer [2005]). The gain in data quality due to, for example, the deployment of borehole receiver arrays, and the common practice of recording the full waveform of the seismic events allows one to process these data sets by applying modern seismic and inversion algorithms.

Over the last 30 years seismic instruments have become significantly improved [Paulsson & Toro, 2002]. This allows one to build seismometers capable of recording signals against background noise, including weak microseismic events that have been indistinguishable before. Moreover, observation and processing practices are also under continuing amendment i.e. recording with an increased number of receivers, improvements of data quality due to application of borehole receivers, utilisation of full waveforms instead of only picked arrival times, etc. The natural seismicity waveform data considered in this chapter was recorded within the main borehole of the San Andreas Fault Observatory at Depth (SAFOD) and serves as an excellent example of such a data set that exhibits the benefits of applying modern technologies Chavarria *et al.* [2007].

There were already several works where the authors used microseismic waveforms to image San Andreas Fault zone. For instance, Chavarria *et al.* [2003] present their results of the imaging seismograms from a number of microearthquakes recorded at SAFOD pilot borehole. Their findings will be used in the following to compare with the results of Microseismic Reflection Imaging. Besides, Zhang *et al.* [2009] use an inverse

scattering method for imaging waveforms of the 575 local microearthquakes recorded at the 68 surface stations. In contrast to my results, Zhang *et al.* [2009] use different seismicity data recorded by alternative acquisition system. Their image reveals several near-vertical reflectors close to the fault zone. The resolution of this image is even lower than active seismic images obtained for this region. For this reason I do not compare the result of Zhang *et al.* [2009] with my findings.

The purpose of this chapter is to show how the Microseismic Reflection Imaging approach can be applied to natural seismicity data. Fortunately, exactly for this part of San Andreas fault zone, there are several active seismic reflection imaging results [Bleibinhaus *et al.*, 2007; Buske *et al.*, 2007]. Since I have both active and passive seismic reflection images of the same area, it is possible to compare the capabilities and limitation of these two methods. Moreover, I will demonstrate how Microseismic Reflection Imaging can contribute to standard active seismic in the task of characterisation of the large fault zone.

3.1   San Andreas Fault Observatory at Depth

The San Andreas Fault (SAF) is a large continental fault located in California, United states. It has length of about 1300 km and was formed by tectonic boundary between the Pacific Plate and the North American Plate. San Andreas Fault zone is one of the main sources of large earthquakes in California. Since 1812 it produces four major earthquakes of $M \sim 7$ and numerous $M \geq 5$ events [Toppozada *et al.*, 2002].

A deep scientific drilling experiment in the SAF zone started in mid 90s. It was aimed to provide data essential to understanding the structure, composition, mechanical behaviour, and physical state of an active plate boundary fault [Hickman *et al.*, 1994]. The San Andreas Fault Observatory at Depth (SAFOD) boreholes are located near Parkfield (California, USA) approximately two kilometres away from the known surface trace of the San Andreas Fault (Figure 3.1). A 2.2 km deep vertical pilot hole was drilled in 2002, followed by the main borehole in 2004–2005, which was drilled vertically down to a depth of 0.9 km where it was deviated and crossed the San-Andreas-Fault reaching a final depth of 2.4 km.
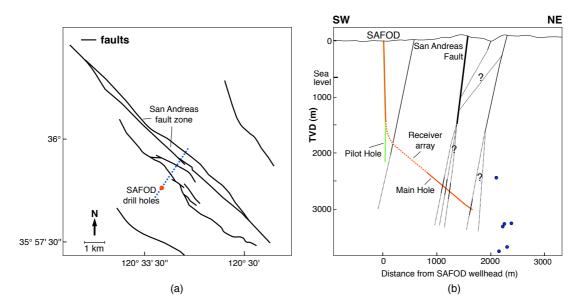
Figure 3.1: (a) Faults map of the area in the vicinity of the SAFOD drill holes (geometry of faults is taken from Bradbury *et al.* [2007]), the blue line represents direction of the cross-section. (b) Fault perpendicular cross-section around SAFOD boreholes (geologic interpretation is taken from Zoback *et al.* [2010]) and location of the 6 earthquakes analyzed further.

3.2 Microseismic data

In the SAFOD area the movement of the SAF is characterised by a combination of repeating microseismicity clusters and aseismic creep [Nadeau *et al.*, 2004]. To monitor the natural seismicity, during one of the several drilling phases in 2005, the main borehole was equipped with an 80-level-3C-borehole-receiver array by Paulsson Geophysical Services (PGS/I) [Chavarria *et al.*, 2007]. The array was deployed in the inclined part of the borehole at a depth interval of 878 – 1703 m below sea level with 15 m receiver spacing. Figure 3.2 shows one of the microseismic events recorded by this borehole array. The data quality allows one to identify different arrivals, including direct P- and S-waves. Besides that, one can also observe the presence of waveforms which can be related to reflected waves. In this study I consider 6 microseismic events, recorded between May 1 and May 8, 2005, in the SAFOD main borehole.
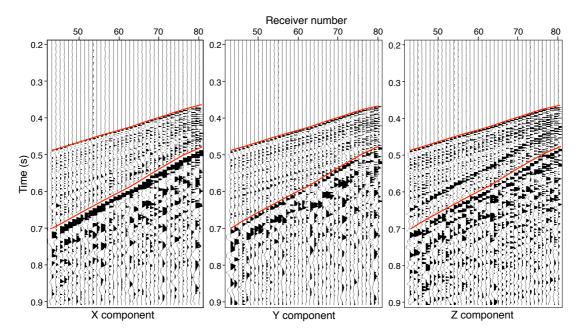
Figure 3.2: Microseismic event recorded by the Paulsson array in the SAFOD main hole at May 4, 2005. The red lines represent the P-and S-first arrivals.

3.3 Location of microseismic events

To locate the microseismic events I used an approach similar to the one proposed in Rentsch *et al.* [2007] with the exception of using the density of the back-propagated rays as the location criterion instead of the stacked amplitude of the image.

The location procedure is schematically shown in Figure 3.3 and includes the following steps:

1. P- and S-wave arrival time estimation. There are several methods to automatically detect P-wave. In this work I apply a straightforward algorithm based on the energy surges analysis of three component (3C) traces. More precisely, of each 3C sample I compute its energy and then search for the moment of time when this energy exceeds the average noise level over some threshold value. To estimate the S wave first arrival times I did manual picking.

2. Direct P-wave polarisation estimation. To obtain the P-wave polarisation, I use auto- and cross-variances of time samples within a time window, including sev-

1. P- and S-wave arrival times estimation

P-wave arrival

energy

time

3C trace energy

S-wave arrivall times estimation – manual picking

time

3c trace #

time

3c trace #

2. Direct P-wave polarisation estimation

time

3c trace #

First arrival time

3C trace   Rectilinearity

0   1

a. Calculate covariance matrix
b. Calculate eigenvalues and eigenvectors
c. Eigenvector corresponding to highest eigenvalues specifies the polarisation

3. Estimation of the event location

Borehole array

Ray paths   Hypocenter

4. Event starting time estimation

Calculation ray travel times (from hypocenter to the receivers)

····· Different rays travel times

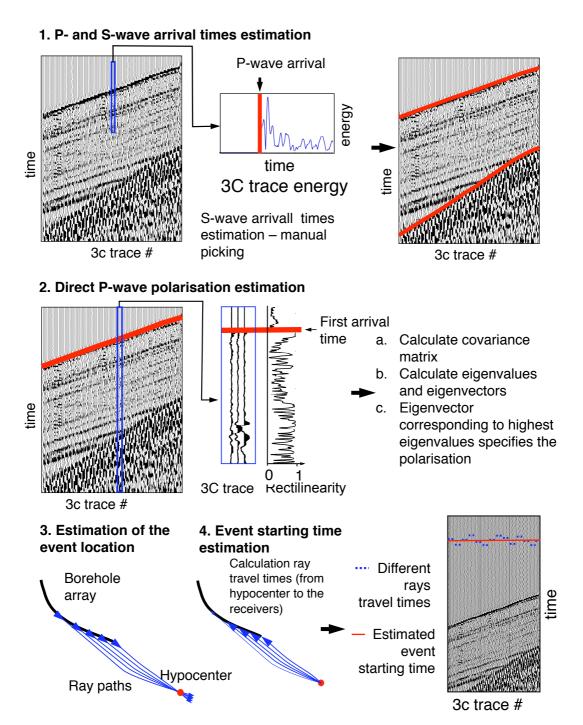—— Estimated event starting time

time

3c trace #

Figure 3.3: Principles of procedure applied to locate SAFOD microearthquakes.

eral dominant periods of the P-wave [Kanasewich, 1981; Jurkevics, 1988]. The eigenvector of the matrix with respect to the largest eigenvalue specifies the current sample polarisation. An additional important result of this procedure is the rectilinearity of the computed covariance matrix eigenvalues. It can be used as a measure of reliability for the obtained direction. While estimating the polarisation for each 3C trace, I calculate the polarisation and corresponding rectilinearity within some time window of the current picked P-wave first arrival time. After that I select the polarisation corresponding to the largest rectilinearity value. Despite possible time picking error, it allows me to obtain a more accurate polarisation value (see Chapter 2 for more details).

3. Estimation of the event location. Having direct wave polarisation values, I can then construct the ray trajectories from the receivers corresponding to the back-propagated direct P-wave [Červený, 2001]. In the case of an accurately estimated polarisation and reasonable velocity model, these ray paths should concentrate at some point corresponding to the hypocenter location. For certain acquisition geometries this approach may fail, for example if the hypocenter is located along the borehole trajectory. In this case all rays are almost parallel and no focused hypocenter can be obtained. To overcome this problem, Rentsch *et al.* [2010] propose to use the time difference between the S- and P-wave arrival times. Following this idea, for each ray I estimate the point at which the time difference between the S- and P-wave arrivals along its path coincides with time difference picked for the current receiver. The central point of the cloud formed from these ray points represents the microseismic source location.

4. Event time estimation. To get the origin time of the event, I calculate the time difference between the picked P-wave arrival time and the P-wave travel time from the receiver to the located hypocenter along the ray path. The triggering time can be estimated as the P-wave arrival time minus these time differences averaged over all receivers.

I applied the described approach to locate 6 considered events. For the location and the following imaging I used the P-velocity model of Thurber *et al.* [2004]. To get the S-velocity model an effective Vp/Vs ratio of 1.83 was used [Rentsch *et al.*, 2007]. Good seismic data quality allowed me to calculate stable and accurate polarisation estimates. While the geometry of the borehole array, particularly with regard to the location of some events, poses difficulties on the location scheme. Since some of the events are
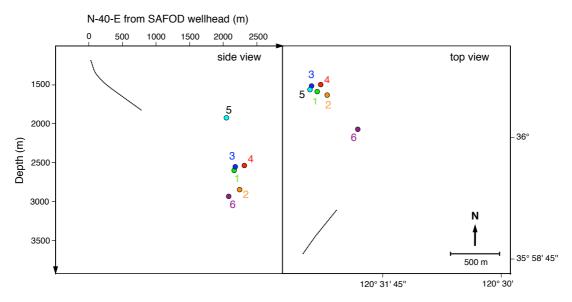
Figure 3.4: Receivers array (black curve) and located microearthquakes.

located along the extrapolated borehole trajectory, the respective ray trajectories are almost parallel. For this case the S-P arrival time difference has been used for locating the events. Final location results are shown in Figure 3.4.

3.4 Imaging results

For the imaging, I only used part of seismic data between P- and S-direct wave arrivals. This data was processed as described in Chapter 2 and then migrated assuming that it is PP reflections. The Fresnel-Volume-Migration images for the six events obtained from the east, north and vertical components, sorted by a recorded signal strength from high to low, are shown in Figure 3.5 (see the respective event locations in Figure 3.4). Despite of the differences, these images reveal the same system of reflectors below the SAFOD main borehole.

Figure 3.6 illustrates an additional 3D representation of the obtained images in the form of an iso-amplitude reflector surface for the five selected events (note, that the image of the sixth event is completely covered by the images of the 5 others, and thus, not seen in this representation). The color of the event sphere relates to the color of the corresponding reflector surface. This representation nicely reveals how iso-surfaces
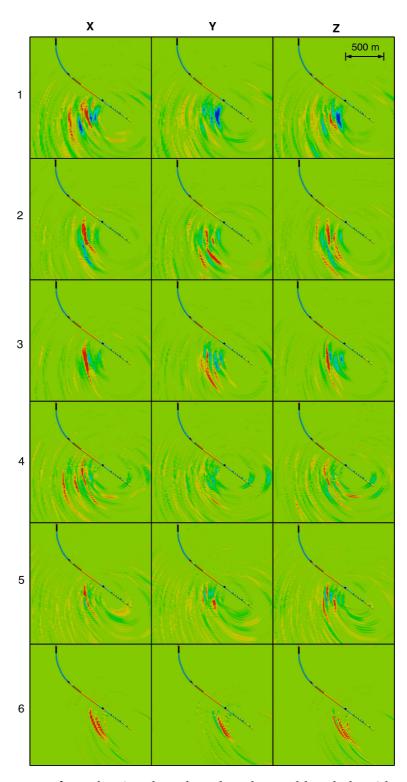
Figure 3.5: Images from the six selected earthquakes and borehole with colour-coded lithology information (east (X), north (Y) and vertical (Z) components), sorted by a recorded signal strength from high to low. See Figure 3.4 with earthquake locations and Figure 3.9 with lithology explanation.
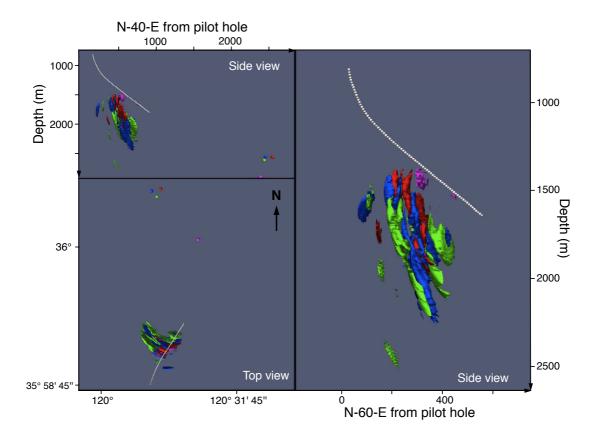
Figure 3.6: Rendered reflector surfaces for five events. The colours correspond to events shown in Figure 3.4.

mainly coincide for all of these five events, although they illuminate slightly different parts of the same reflectors.

Besides that, I constructed the stacked image of the six images for all three components separately. A cross section of stacked images is shown in Figure 3.7. One can see that the resulting images are partially similar to each other, while in some other parts they are clearly complementary. In addition to the strongest reflectors presented in Figure 3.5, several less pronounced reflectors appeared at larger distances from the borehole. The solid black lines in Figure 3.7 summarise these reflectors as an interface map obtained from the stacked sections of the three migrated wavefield components.
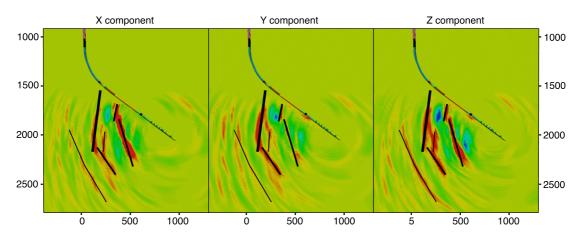
Figure 3.7: Cross section of the stacked image obtained from the east (X), north (Y) and vertical (Z) components for the six events. Thin solid black lines - obtained interface map.

3.5 Comparison with other imaging results

Several active- and passive-source seismic imaging investigations around the SAFOD site have been presented earlier in the literature. In this work, I compare my findings to the following studies. I considered result of Chavarria *et al.* [2003] who used microseismic reflection data recorded at SAFOD pilot borehole to image the same part of the San Andreas Fault. For comparison I also used imaging results of surface reflection seismic obtained by Buske *et al.* [2007] and Bleibinhaus *et al.* [2007].

In Figure 3.8 one can see four panels containing the vertical component of the stacked image (Figure 3.7) and results obtained by Chavarria *et al.* [2003], Buske *et al.* [2007] and Bleibinhaus *et al.* [2007] presented in the same scale in the direct vicinity of the SAFOD main borehole. Obtained interface map (see Figure 3.7) is presented over each of these panels.

Chavarria *et al.* [2003] apply a Kirchhoff migration to the waveforms recorded from numerous microearthquakes at the SAFOD pilot borehole (Figure 3.8b). Microearthquakes are located within the San Andreas Fault zone with the depths varying roughly between 1 to 7 km below sea level. For comparison I used their PP reflections migration result for the vertical component seismograms from hypocenters located ≤ 2 km from the pilot hole. This was motivated by the fact of geometric similarity to this study. Although the dip and shape of some sub-horizontal reflectors demonstrates a similar trend, the
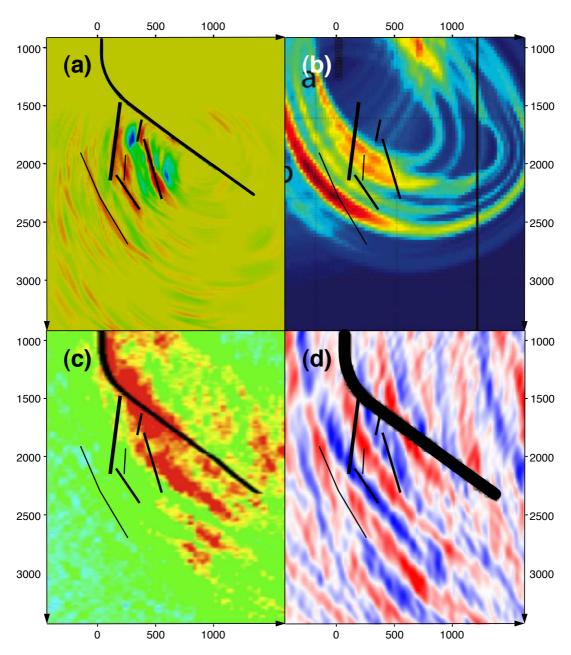
Figure 3.8: (a) Vertical component of stacked image. (b) Image from Chavarria et al. [2003]. (c) Image by Buske et al. [2007]. (d) Image by Bleibinhaus et al. [2007]. Thin solid black lines - obtained fault map (see Figure 7).

matching reveals significant differences. The possible reason for this is an inaccuracy in the events location and limited aperture because of use of the vertical pilot hole data in Chavarria *et al.* [2003]. Despite the fact that the same velocity model [Thurber *et al.*, 2004] was used in both studies, the divergence can also take place due to some inconsistencies in different parts of this model. Such inconsistencies can impact on the results because these two imaging methods used data recorded by different acquisition systems.

Buske *et al.* [2007] apply the Fresnel-Volume-Migration technique (the same as I employ for Microseismic Reflection Imaging) to the SAFOD2003 surface reflection seismic data set. In their image red- and yellow- coloured areas correspond to increased reflectivity (Figure 3.8c). In general, the image represents a low resolution (large-scale) structure of the fault system consisting of several fault branches with different dips and reflection strengths. Comparison of the images presented in Figures 3.8a and 3.8c show some differences but basically both images demonstrate a similar trend in the transition from a sub-vertical to a sub-horizontal direction, inclined at a similar angle. Moreover, result of the Microseismic Reflection Method provides higher image resolution, and instead of a smooth zone of high reflectivity shows the fine-scaled structure inside the fault zone, perhaps related to second-order faults encountered along the borehole.

Bleibinhaus *et al.* [2007] perform the steep-dip pre-stack migration with the same SAFOD2003 data set as was considered in Buske *et al.* [2007]. The major difference between the images is the absence of the sub-vertical reflectors in Figure 3.8d. The other inclined parts of the reflectors basically match quite well.

Passive and active imaging results may supplement each other at different scales: the surface seismic images obtained from lower frequency signals provide information about the large scale structure of the fault system, whereas the images obtained by using the high frequency microseismic events support these findings, helping to understand the complex fine-scale structure of these reflectors. In particular, this holds for highly reflective parts where separate reflectors cannot be easily resolved from the surface seismic image. Furthermore, the consistency of these images proves the accuracy of the microseismic event location procedure and the corresponding polarisation estimation.

3.6   Correlation with geology

I also attempted to find the relationship between the obtained reflectors and lithology along the SAFOD main borehole (Boness & Zoback [2006]). Figure 3.9 shows the image obtained for the vertical component of the stacked image and supposed interface map (see Figure 3.7) together with the SAFOD main borehole trajectory and corresponding lithology. There are several evident reflectors in the vicinity of the borehole. The first reflector (from the left to the right) crosses the borehole at around 1900 m measured depth (MD) along the borehole trajectory, and likely corresponds to the interface between granodiorite and bredicated granite which is represented by a thin fault layer. The second reflector intersects the borehole at level 2280 m MD. This level does not correspond to any of the interfaces, but it is located inside the fractured sandstone layer. Probably this reflector can be interpreted as a second-order fault inside the fractured sandstone bedding. The last spot of high reflectivity in the image, in the vicinity of the borehole at 2620 m measured depth, may be related to a thin fault layer at this level of the lithology log.

One of the recent works that represents the current level of understanding of the geological structure of SAFOD is a paper of Zoback *et al.* [2010]. In their interpretation, there is a single major fault in the area of interest, which is Buzzard Canyon fault. This fault is inclined at an angle of about 13 degrees from the vertical, going directly from the surface, crossing the SAFOD main borehole and continuing under level of a 2500 m depth. The strongest sub-vertical reflector in the obtained image (Figure 3.7) seems to correlate well with this fault. Furthermore, the image may be an indication of a possibly more complex structure of the Buzzard Canyon fault. This complexity is expressed in the curvature of the main trace of the fault, and the presence of the second-order faults seen as weaker reflectors. The other three images by different authors (see Figures 3.8b, 3.8c and 3.8d), in spite of their differences, also indicate such a possible complexity of the fault.
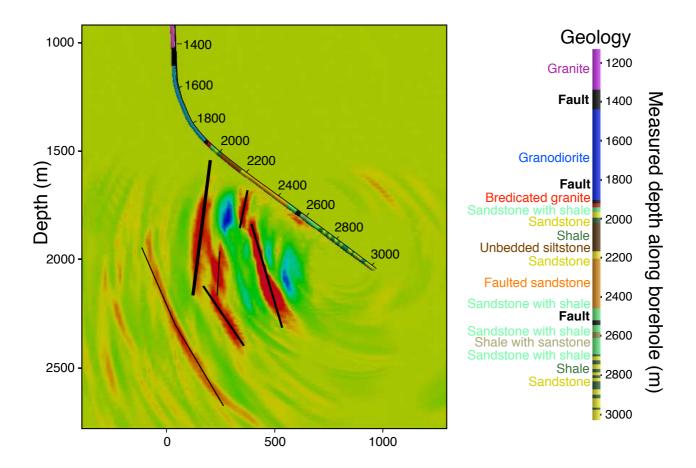
Figure 3.9: Vertical section of stacked image and lithology correlation. Solid lines represent supposed reflectors map (see Figure 3.7).

3.7   Conclusion

In this chapter I have presented the application of Microseismic Reflection Imaging to the natural seismicity data. Using polarisation of the P-wave first arrivals, hypocenters of the microseismic events have been precisely located. Then these events are treated as "pseudo-active" seismic sources and reflections within the recorded wavefield are processed by using a directional migration algorithm. As a result, well-resolved images of the fault branch vicinity near the borehole were obtained. Moreover, due to the presence of the events illuminating different parts of the fault, suggested reflectors network were constructed. A comparison of these findings with existing seismic reflection images, as well as with the borehole lithology, shows a fairly satisfactory agreement. To conclude, the obtained results contributed to the spatial characterisation of the internal structure of the SAF.

In the next two chapters I consider seismicity induced by fluid injections. These datasets use different acquisition geometry: both are recorded at several individual deep and shallow borehole sensors. Furthermore, the number of detected and located events is much larger than in the case of SAFOD data.

REFLECTION IMAGING USING SEISMICITY RECORDED AT A SINGLE BOREHOLE SENSOR

In order to check the robustness of the microseismic reflection method it is reasonable to test it at extreme operating parameters. One of the critical parameters for the method is the acquisition aperture size. If the aperture is low, each microseismic source illuminates a very narrow subsurface area and therefore the position of each particular reflector cannot be confirmed by stacking images for many events. In this situation it is problematic to get a reliable image. Other important factors are the amount of data and the data quality. Generally, the worse microseismic data, the more data needed to get a distinct image of reflectors.

In this chapter I consider the microseismic data obtained from the German Continental Deep Drilling program (KTB). For the imaging I use about 50 microseismic events recorded at the single three component downhole sensor. This shows the abilities of the method in the situation of extremely low aperture and a small amount of relatively weak and noisy reflection data.

4.1 KTB project

The German Continental Deep Drilling program is the project aimed to investigate the structure and processes in the continental crust using a deep (9.1 km) borehole.

The main research topics included studying the geophysical and thermal structure of the crust, crustal stress field, crustal fluids and transport properties, and evolution of central European Variscan basement [Emmermann & Lauterjung, 1997].

The KTB site is located in South-East Germany near the western margin of the Bohemian Massif. Two boreholes were drilled. The pilot hole was drilled in 1987 – 1989 and reached the depth of 4 km. Drilling of the main hole was finished in 1994 at a depth of 9.1 km. In order to investigate the crustal stress field and the fluid transport properties, two short and long term fluid injection experiments were carried out between 1994 and 2005 [Zoback & Harjes, 1997; Baisch *et al.*, 2002; Gräsle *et al.*, 2006].
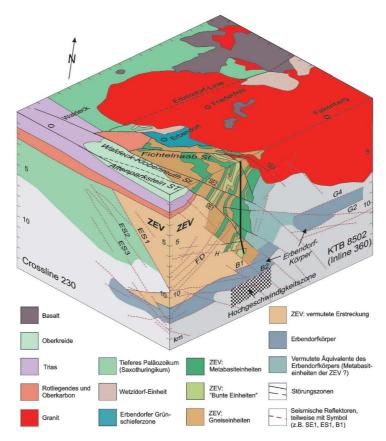

Figure 4.1: Schematic geological representation of the KTB site. (Figure is taken from Harjes *et al.* [1997])

Hirschmann [1996] outlined results of geological interpretation obtained from seismic investigations, drilling logs and surface geology (Figure 4.1). According to the author, there are two dominant north-east dipping fault zones referred as SE1 and SE2

encountered by the main hole at 7.2 and 4.0 km depths respectively.

4.2 Microseismic data

In this study I consider the data from 2004/2005 long term fluid injection experiment [Shapiro *et al.*, 2006]. Starting in 2004 for over ten months, 84.600 m^3 of water were continuously injected in the open-bottom section of the KTB pilot hole at $4\,km$ depth, directly to the SE2 fault zone. Injection rate was constant at $200\,l/min$, interrupted by several short-term pump failures. The injection was preceded by one year fluid extraction phase in 2002/2003 (Gräsle *et al.* [2006]). No seismicity related to the water extraction was observed. Detectable induced microseismicity commenced during the injection test, when the volume of previously extracted water was compensated (Shapiro *et al.* [2006]).
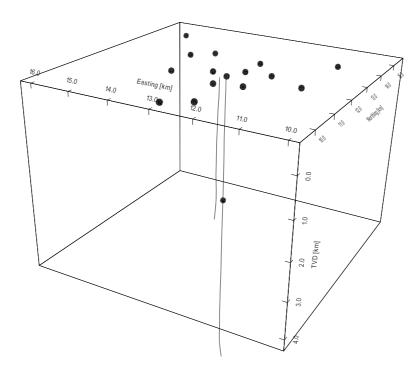

Figure 4.2: KTB acquisition geometry. Black spheres – sensor positions, black solid lines – main and pilot boreholes geometry.

The seismicity was monitored by a seismic network with a variable number of near-surface stations (on average 10–15 stations). Most of the stations were installed within

a radius of $3\,km$ from the KTB site (Figure 4.2). Additionally, there was a borehole seismometer installed in KTB main hole. During the monitoring period there were four positions of borehole sensor at 1950, 3500, 3485 and 3476 m depth. All instruments were 3-component seismometers and data were recorded continuously at sample rates of $200\,Hz$ for the surface stations and at $1000\,Hz$ for the borehole sensor. Monitoring of seismic activity hast been continuing for almost two years, started six months before beginning of the injection and ended four months after stop of the injection.
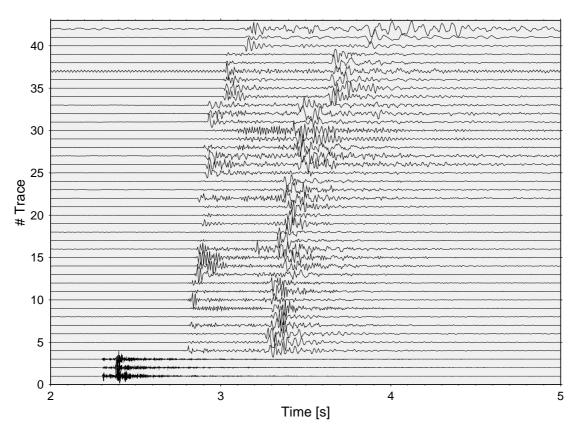

Figure 4.3: Example of a microseismic event recorded by both borehole sensor (traces 1–3) and surface receivers.

An example of an event recorded at both surface and borehole receivers is shown in Figure 4.3. Seismicity occurred in the vicinity of the downhole sensor and therefore quality of the signal recorded at the borehole seismometer is much better compared to the surface network.

The cumulative number of events detected by near-surface stations is 146, and more than 3000 for the borehole sensor [Kummerow *et al.*, 2006b]. All events are small with magnitudes in the range of −3.7 to +0.3 [Haney *et al.*, 2011]. In this study, I consider the data recorded during the third installation of the borehole sensor at 3485 m depth and approximately 540 m away from the injection point. This position is characterised by the largest number of detected (1846) events [Kummerow, 2010].

4.3   Microseismicity location

The absolute location of the induced events was performed by Kummerow *et al.* [2006a]. The first arrivals in the data from both borehole and surface sensors have been manually picked. To improve location accuracy, the authors computed differential travel times using waveform cross-correlation and combined them with the original time picks. Applying the algorithm adapted from Shearer [1997], they obtained adjusted and more consistent time picks. The location was performed using NonLinLoc grid-search algorithm [Lomax *et al.*, 2000]. Finally, locations were refined by the double-difference method [Waldhauser & Ellsworth, 2000; Waldhauser, 2001]. For location a velocity model with constant V_P/V_S ratio of 1.72 has been used. Mean RMS residual of the location was ~ 6 ms [Kummerow *et al.*, 2006a] with absolute location error of 50–100 m [Kummerow, 2010].

The hypocenters of 58 located events as well as the borehole sensor and the injection point positions are shown in Figure 4.4. The microseismic cloud has an elongated NW-SE trending shape approximately 250 meters away from the injection point. These events are used for the reflection imaging in the following.

Kummerow [2010] also considered weak events that were detected by the borehole sensor but not observed by the surface network. To do this, the author applied the correlation-coefficient based location approach. Using pre-located strong reference events and waveform similarity between events as a measure of distance between hypocenter, additional 954 microearthquakes were localised. Located events were characterised by local magnitudes less than -1.5 [Kummerow, 2010] and rather small signal-to-noise ratio. This makes waveform polarity estimation quite problematic. Moreover, these events have larger location uncertainty. For these reasons, I did not use this additional data for reflection imaging.
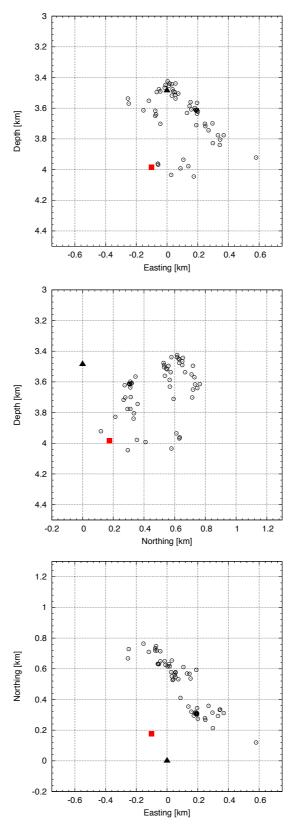
Figure 4.4: Location of 58 microseismic events recorded by borehole and surface sensors. Circles – events, triangle – borehole sensor, red square – injection point.

4.4 Common-receiver gather

Due to the limited amount of data, I did not perform event selection as it was described in Chapter 2, Section 2.4. I used the data recorded at borehole sensor from all 58 located microseismic events to produce the common-receiver gather (Figure 4.5).
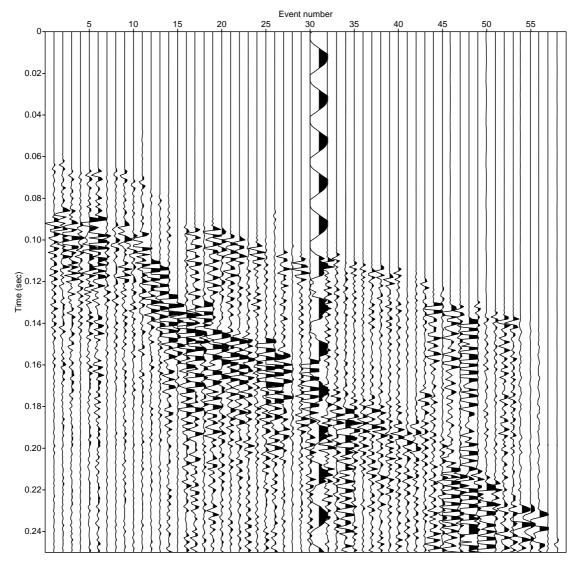

Figure 4.5: Vertical component of the seismic gather produced from 58 located microseismic events recorded at the borehole sensors.

The direct P- and S- waves are clearly observable from the data, but there are no distinct events that can be interpreted as reflections. Although, at some traces one can spot

events between the direct waves as well as after S-direct wave. Anomalous signal at the trace #30 can probably be explained by the temporal malfunction of the borehole sensor. This particular event was located and therefore included to the gather because at two other components it was possible to detect arrival times of the direct waves. However, due to waveform polarity estimation procedure (see Chapter 2, Section 2.5) this seismogram did not contribute to the final image. Generally, strong noise at one of the components introduced significant bias to the hodogram making it non-linear. As a result, linearity of hodogram R became low for the complete time interval and the corresponding trace was automatically excluded from the imaging process. In the situation of strong coherent noise, the signal is linear. Obviously, it provides biased polarity estimates. In this case, corresponding trace may contribute to the image and therefore should be excluded manually.

4.5   Imaging results

Since the data quality is rather poor, it was quite hard to estimate polarity of the wavefield. In most cases direction of wave propagation for S-waves is less accurate and therefore more demanding to the data quality compared to directivity estimates for P-waves. For this reason, I only performed imaging of reflected P-waves. Moreover, to make the result more stable I used only part of the data between the direct P- and S-waves which was interpreted as PP reflections. For the same reason, in the imaging procedure, I stacked the absolute values of amplitudes.

The distance from the borehole sensor to the cloud is in the range of 200 – 600 m (see Figure 4.4). Accordingly, PP reflections arriving before direct S-wave can potentially illuminate only a close vicinity of the borehole sensor. For that reason I used a limited imaging volume: a cube with side length of 1200 m and 2 m grid spacing (see Figure 4.7). The volume includes the microseismic cloud, borehole sensor and injection source.

The obtained stacked image for all event-receiver pairs is shown in Figures 4.6 and 4.7. In the vertical section one can see several parallel reflectors in the image. Resolution of the image is quite high due to the high frequency of reflection data. The reflectors have slightly curved shape. Such curvature of the reflectors can be explained by the nature

of Kirchhoff pre-stack migration[1], where amplitudes are stacked along isochrones (see Chapter 2, Section 2.6 for more details) which have elliptical shape. For wide angle data it is compensated by stacking of images from neighbour receivers. In this case, constructive interference is enhancing the reflectivity at true position of the reflector. However, in the situation of a limited aperture and a low spatial coverage, an image of a flat reflector inevitably becomes curved. In spite of that, one can identify the system of planar reflectors with dip angle of around 60 degrees. The dip of the reflectors is close to the dip of the cloud (see Figure 4.6).
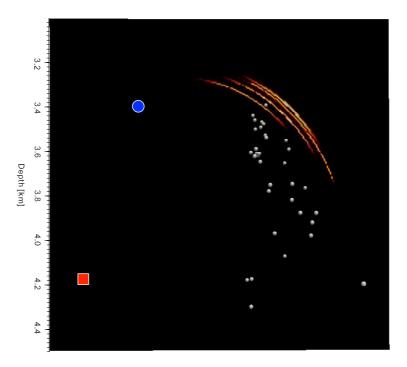

Figure 4.6: Image of the PP reflected waves from 58 events (vertical section). Blue circle – borehole sensor, red square – injection point, gray dots – microseismic events.

From Figure 4.7 one can see that all the reflectors are located at the edge of the cloud, which is opposite with respect to the receiver. There could be other reflectors inside the cloud or closer to the receiver. Unfortunately, due to the relative position of the sources and receiver and the small number of events used for the imaging it is hardly possible to illuminate this area by PP reflected waves. For the same reason, it was only possible to construct the image of a small part of the bigger structure at 3.2 – 3.8 km depth interval.

---

[1]The Microseismic Reflection Method uses Fresnel Volume Migration, but the basis for this imaging algorithm is Kirchhoff migration.

The revealed system of nearly planar parallel reflectors with the same dip seems to be repetitive. The distance between neighbour reflectors is in the range of 20–40 m, which is even smaller than location misfits (see Section 4.3). Thus, most likely imaged system of reflectors is stacked images of the same reflector illuminated from different sources with inconsistent relative positions. Inconsistency of event locations results in inconsistency of reflector position on the images for individual events. Consequently, instead of enhanced reflectivity at true position of the single reflector, the image shows multiple parallel reflectors with comparable levels of reflectivity. Nonetheless, even in the situation of low signal-to-noise ratio, images from various source-receiver pairs appear to be quite consistent and position of the reflector can be reconstructed with the accuracy of microseismic event location.
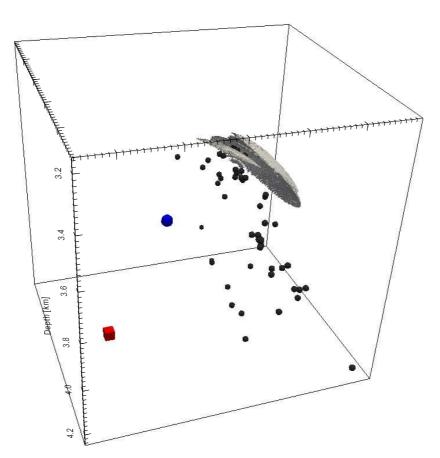

Figure 4.7: 3D representation of the strongest reflectors from the obtained image. Blue circle – borehole sensor, red square – injection point, black dots – microseismic events.

4.6   Comparison with active seismic imaging results

Buske [1999] performed 3D prestack Kirchhoff migration of active seismic survey data (ISO89-3D dataset) which was recorded in the vicinity of KTB boreholes. The lateral size of the survey area was 21 km x 21 km. The dataset included recorded traces from more than 3000 Vibroseis shots. The waveforms from all the available shots were migrated separately and stacked in the imaging volume of 21 km x 21 km x 15 km.

The migrated volume revealed the geometry of the two dominant geological structures in the area: SE1 fracture zone at 2–8 km depth interval and deep highly reflective area known as the Erbendorf body at depth below 10 km. The authors also estimated the dip angle of SE1 fault as around 55 degrees.

Jaya *et al.* [2009] analysed seismic attributes calculated from the 3D prestack Kirchhoff migration image of Buske [1999] with the aim to enhance specific geological structures which may not be visible in the original image. The seismic attributes were computed in the form of absolute values of the Hilbert transform of the migrated seismic data. In addition to previously shown geometry of the SE1 fault zone, the second weaker reflector corresponding to the SE2 fault was revealed at 3–5 km depth. Vertical and horizontal sections of the seismic attributes volume are shown in Figure 4.8[1]. From the sections one can see distinct representation of NW-SE elongated and almost parallel the SE1 and SE2 fault zones. Shapiro *et al.* [2005] observed that the induced seismicity is directly related to the SE2 reflector. Their interpretation was that the seismicity is guided by the fault system because it is characterised by enhanced permeability due to fracturing. The spatial relation of microseismicity and SE2 fault zone is even clearer from the seismic attributes analysis (see Figure 4.8).

In Figure 4.9 one can see the fragment of the vertical section of seismic attributes and the position of the strongest reflector obtained by means of the Microseismic Reflection Imaging. The reflector is located inside the zone of high reflectivity in the active seismic image that is associated with the SE2 reflector. Despite of the fact that the microseismic image reveals only a small part of the large geological structure, the correlation of this reflector with the SE2 fault zone in the seismic attributes image is evident by the dip angle and position.

---

[1]Here I show not the complete migrated volume but only the part that is centred to the area of interest of this work
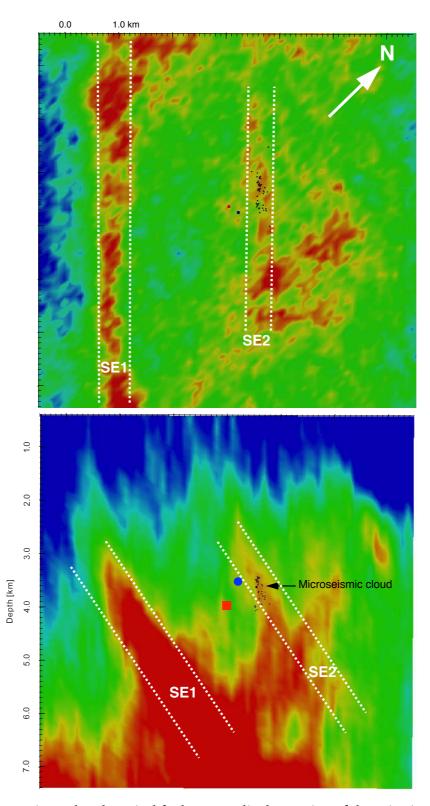
Figure 4.8: Horizontal and vertical fault-perpendicular section of the seismic attributes cube obtained from surface seismic imaging. Both sections are crossing the borehole sensor position. Black dots – 58 located microseismic events, blue dot – borehole sensor, red dot – injection source position.
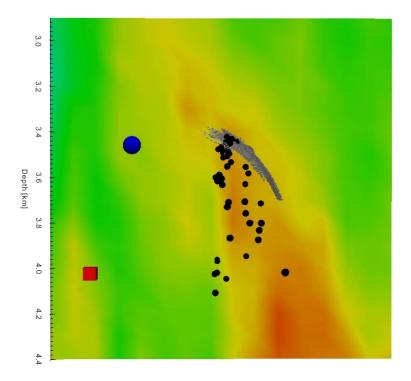
Figure 4.9: Comparison of the seismic attributes obtained from the surface imaging results (on the background) and the reflector obtained by Microseismic Reflection Imaging (gray surface). Blue circle – borehole sensor, red square – injection point.

4.7   Conclusion

This chapter shows how microseismic reflection imaging works for extremely restricted input parameters. In the situation of a small amount of weak reflection data one can hardly expect to get a detailed image of the target area. Nevertheless, low quality input data did not introduce significant migration artefacts or distorted reflectors. Particularly, the method extracts the reliable part of the reflection data and constructs the image.

The obtained image can unlikely be considered as informative for the characterisation of the fault zone. However, it shows that even weak seismicity data contains information that can be used to spot reflectors inside a seismically active area.

In the next chapter I also consider induced microseismic dataset. It also has a restricted aperture, but in contrast to the KTB data, it includes several thousands events with much better signal to noise ratio.

REFLECTION IMAGING USING SEISMICITY INDUCED BY AN EGS STIMULATION

The use of fluid stimulation is an important issue in the development of unconventional reservoirs in the oil & gas industry and in the creation of enhanced geothermal systems (EGS). As a result of treatment, elevated fluid pressure penetrating through the rock and interacting with fluid pressure in the pores and pre-existing fractures can lead to sliding along these pre-existing or newly created fractures and inducing microearthquakes [Nur & Booker, 1972; Shapiro *et al.*, 2005]. The induced seismicity can potentially be used as sources for reflection imaging.

In hydrocarbon exploration fluid injections are used, for example, for hydraulic fracturing. Fracking is a stimulation technique aimed to increase reservoir production rate by creating new fractures that provide a permeable path connecting a production well with a reservoir [Economides & Nolte, 2000]. It is typically applied to reservoirs that cannot be produced at economic flow rates without massive treatment. Examples of such reservoirs are gas shales, tight-gas sands, heavy oil and coalbed methane [Holditch, 2003]. As volumes injected during hydrofrac operations are usually small and stimulations are short in time, the induced seismicity has relatively low magnitudes [Shapiro *et al.*, 2010].

EGS produce the heat energy by circulation of water through the hot (T > 100° C) rock at depth (Z > 3 km) (e.g. Ripperger *et al.* [2009]). Typically, the target rock is not porous and the water flow passes through natural fractures, which implies low

permeability. Hydraulic stimulation is commonly used to increase permeability and to achieve reasonable flow rates. Such stimulation leads to producing numerous microseismic events and, with non zero probability, a few small earthquakes that can cause some damage at the surface [Giardini, 2009].

In this chapter I consider the injection-induced microsesmic data from the EGS project in Basel, Switzerland [Deichmann & Ernst, 2009]. This dataset includes several thousands of microseismic events and is characterised by high quality seismograms recorded by downhole instruments. These instruments are installed at different distances from the stimulation point [Häring *et al.*, 2008]. This allows me to probe the capabilities of the method and determine under what conditions it is possible to get reasonable results.

To my knowledge, there were already two attempts to use waveforms from microseismic events induced during the stimulation of the Basel EGS for the reflection imaging.

Dyer *et al.* [2008] present the 3D stack-type migration applied to the microseismic data recorded at one of the sensors. Since the polarities of reflected waves were not taken into account, the obtained images appeared to be numerous circular structures covering most of the imaging volume. In order to make the result more consistent with maximum horizontal principal stress and spatial distribution of the events, the authors apply aperture control and constrained the azimuth and dip of the reflectors. Their final result reveals the large-scale steeply dipping structure in the western direction outside of the seismically activated zone.

Asanuma *et al.* [2011a] apply the Acoustic Emission reflection method introduced by Soma *et al.* [2002a] and used multiple events as sources for imaging. They identify reflected phases by the analysis of 3D hodogram in the time and frequency domains and stack a coherence index on a restricted iso-time-delay surface. The surface is restricted by the polarization of reflected waves and the relative time of reflected phase of other members of the same multiplet [Tamakawa *et al.*, 2010]. Highly reflective areas in their image are located around the microseismic cloud, the most distinct reflector appears to be approximately 1 km to the West from the injection point.

The purpose of this chapter is to demonstrate how the Microseismic Reflection Method can be applied to microseismicity triggered by fluid injection. The ultimate goal is to get an image of the stimulated reservoir interior, which can be helpful in further under-

standing of processes controlling nucleation of induced seismicity. In Reshetnikov *et al.* [2011] I and the co-authors presented the microseismic reflection image of the large-scale fault at about 1 km to the West from the reservoir. In Asanuma *et al.* [2011a], the authors reveal that their image is in good agreement with MRI result. However, this structure is not a focus of this work and therefore this result will not be included into this work. For the same reason, the results of this work cannot be directly compared to the previous studies.

5.1 Enhanced Geothermal System at Basel

The project

The active phase of the geothermal project in Basel, Switzerland was started in 2006 with the aim to build a plant producing both electricity and heat directly in an urban area. A real-time microseismic monitoring network was installed containing a number of shallow and deep borehole sensors. The stimulation well Basel 1 was drilled to a total depth of 5 km [Häring *et al.*, 2008].

In order to enhance permeability of the granitic basement, Basel 1 well was stimulated with a total amount of 11,570 m^3 of water. After 6 days of stimulation (2–8 December 2006), it was stopped due to unexpectedly high microseismic activity with event magnitudes up to M_L 2.6 causing some minor damage at the surface. However, activity remained significant and decreased slowly. Up to the end of November 2007, multiple events were recorded with the maximal occurred magnitude M_L 3.4 a few hours after the stop of injection [Häring *et al.*, 2008].

Later, after the independent seismic hazard risk analysis, the local authorities decided to completely stop the project [Bachmann *et al.*, 2011]. Nevertheless, the microseismic events recorded at the Basel microseismic monitoring system represent a great opportunity for further understanding the physics of induced seismicity.

Geological settings

The Basel geothermal site is located in the southern part of Upper Rhine Graben, which is the part of European Cenozoic rift system. Locally, this area is characterised by several NNE-SSW and NW-SE fault systems of various ages in the eastern part [Dyer *et al.*, 2008]. Since 1975 10 events with $1 \geq M_L \geq 2$ and 15 events with $M_L \geq 2$ were registered in this area [Häring *et al.*, 2008].

The well Basel 1 was drilled through 2411 m of sediments (Quaternary, Tertiary, Mesozoic and Permian), approximately 100 m of Permian siltstone and weathered granite, followed by 2493 m of crystalline basement. The basement rocks for more than 99% consist of granite [Häring *et al.*, 2008].

The frequency and orientation of the pre-existing natural fractures in the basement were determined by acoustic borehole images. In total 984 fractures were found [Häring *et al.*, 2008]. The detected fracture density at the lower part of the borehole, including the open hole section was detected as 0.2-0.3 per meter. The dominant orientation of natural fractures was NW-SE to NNW-SSE, with steep dips exceeding 60° [Häring *et al.*, 2008].

The principal stress direction was estimated from the log analysis in the granitic basement. The direction of SHmax was estimated from borehole breakouts as $N143 \pm 14°E$ and from induced tensile fractures as $N151 \pm 13°E$ (Dyer *et al.* [2008]). The regional direction of SHmax was also determined by Plenefisch & Bonjer [1997] as 150°.

Hydraulic stimulation

As indicated in Häring *et al.* [2008], massive stimulation of the Basel 1 well continued for 6 days, starting on December 2nd, 2006. Flow rate was increased from 0 up to 3300 L/min resulting in a wellhead pressure of 296 bar. In total, 11,570 m^3 of water was injected. Growing of the flow rate was accompanied by increasing of seismic activity. On December 8, 2006 when the activity reached unacceptably high level and the stimulation was completely stopped.

Basel earthquake magnitudes were determined by the Swiss Seismological Survey. The

biggest event registered during the period of the injection had magnitude M_L 2.8. However, even after the injection has been stopped, occurrence rate of the events $M_L > 1$ remained relatively high. Moreover M_L 3.4 event was detected. In order to weaken further seismic activity project the operator decided to bleed-off the well. As a consequence the pressure dropped to hydrostatic condition within 4 days (see Figure 5.1).

The first induced microseismic event was detected nearly 4 hours after the start of the Basel 1 well treatment. In total, during 6 days of the stimulation 11,200 events were detected. After stopping the injection, seismic activity remained high and up to the end of November 2007, about 3700 more events were recorded [Häring *et al.*, 2008]. I this paper I consider 3068 events, which occurred during both injection and post-injection phases.
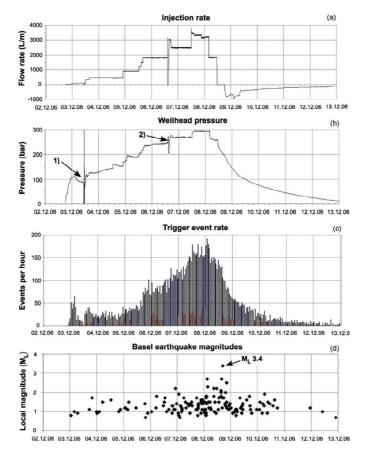

Figure 5.1: Data on the hydraulic stimulation of well Basel 1 (Figure is taken from Haring et al. [2008]). History of (a) injection rates, (b) wellhead pressures, (c) trigger event rates and (d) Basel earthquake magnitudes as determined by Swiss Seismological Survey (SED).

5.2 Microseismic data

The data used in this study was generously provided by Prof. Dr. Hiroshi Asanuma from Tohoku University, Sendai, Japan. This dataset includes a number multicomponent traces for six borehole sensors containing pre-detected microseismic events. In total, 3068 recorded events were provided. The length of each seismogram is 6 seconds.

Microseismic monitoring system

The microseismic waveforms produced during and after reservoir stimulation were recorded by several networks operated by independent institutions. Here I consider the network operated by Geothermal Explorers Ltd.. This network includes six three-component downhole sensors in long-term operation shown in Figure 5.2. The coordinates as well as distances from the injection point can be seen in Table 5.1.
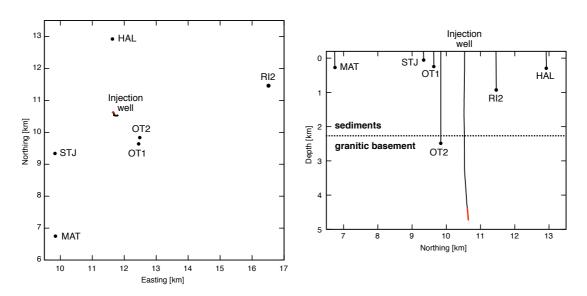

Figure 5.2: Distribution of downhole sensors, left: map view; right: side view. Black dots – borehole sensor positions, black solid lines – boreholes, red solid line – injection well open hole interval.

Table 5.1: Coordinates of the borehole sensors and distances for the injection interval.

Name	X [m]	Y [m]	Depth [m]	Distance [km]
OT2	12486	9838	2487	2.2
OT1	12452	9638	247	4.3
HAL	11630	12922	297	4.7
STJ	9833	9340	56	4.9
MAT	9848	6750	274	5.9
RI2	16514	11459	928	6.0

There are five shallow stations installed in the sedimentary layer: STJ, MAT, HAL, OT1 and RI2. There is also one deeper geophone OT2 located in the crystalline basement at 2740 m depth 2 km SE from the treatment borehole. One more additional downhole sensor was temporarily installed in Basel 1 treatment borehole. However, it broke just after the start of the treatment and the corresponding data are omitted here. The sampling rate for all sensors is 1 ms.

Microseismic waveforms

An example of the raw microseismic waveforms recorded at 6 sensors is presented in Figure 5.3. This event was recorded at 08 Dec 2006, 01:30 and shows the common high signal quality among the analysed data. All the downhole sensors recorded three component traces. The deepest OT2 geophone has a regular orientation with two axes oriented horizontally and the third one vertically, while all other stations use Galperin sensor orientation [Galperin, 1955, 1985].

Due to the different distances between the sensors and the injection interval, the frequency content and the amplitude ranges vary for different 3C traces. Nevertheless, in many cases the quality of the data allows one to identify direct P- and S- arrivals for all 6 station recordings. There are also some quite strong phases that are not associated with the direct waves. This can be an indication of reflections within the traces, which would imply the presence of reflective objects in the close vicinity of the events.
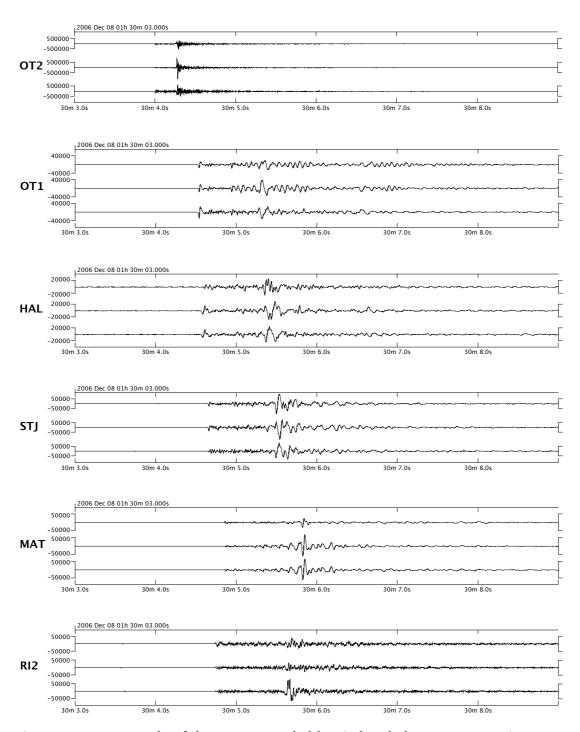
Figure 5.3: An example of the event recorded by six borehole sensors. Receivers are sorted according to the distance from the injection interval. Amplitude units are given in micro volts [uV].

5.3   Location of microseismic events

In the case of the EGS in Basel, the microseismic monitoring system provides a good spatial coverage of the stimulated reservoir (see Figure 5.2). Therefore, a location algorithm based on a grid search is applicable. In order to take advantage of the high quality seismic data (see Figure 5.3), the algorithm presented in Kummerow [2010] and Kummerow & Shapiro [2010] is used in the following.

This location algorithm requires the P- and S-waves first arrival time picks. In order to achieve maximal accuracy all the data were picked manually. Due to strong high-frequency signal, the average picking accuracy for OT2 station is estimated to be about 1 ms. For other stations depending on strength of a signal it reaches up to 5 ms, but in average is in the limit of $1 - 3$ ms (J. Kummerow, personal communication).

The complete workflow of the location process is described in Kummerow *et al.* [2011] and consists of four steps:

1. Using obtained P- and S-phase picks, events with similar waveforms are identified as event multiplets. Correlation between traces is computed for picked data at all stations. The length of the P and S time windows is 180 ms. Two events are identified as multiples if their average correlation value larger than $C_{min} = 0.85$ for 3–80 Hz bandpass-filtered data.

2. Information about events clustering is used to adjust the original hand picks for each multiplet. Time picks are corrected by relative time measurements between event pairs and further refined by removing the relative time lag between particular trace and summation trace, which is obtained by stacking the best correlated traces in the cluster (Kummerow *et al.* [2012]).

3. Further, the grid-search algorithm (NonLinLoc, Lomax *et al.* [2000]) is applied to locate the microseismic events using adjusted P- and S-wave time picks.

The velocity model used in this study consists of two layers of sediments and the granitic basement with the interface at 2265 m below see level. Average P- and S-velocities for each layer are determined from the sonic velocity measurement by Dyer *et al.* [2008] and given in Table 5.2. Such simple velocity model can potentially cause

Table 5.2: Velocity model of EGS in Basel

Layer	Depth (m)	Vp (m/s)	Vs (m/s)
Sediments	0–2265	3980	2080
Granitic basement	2265–5000	5940	3450

significant location errors. To compensate for the local velocity variations, static corrections are introduced (constant time shifts of all seismic traces recorded at a particular borehole sensor that are supposed to reduce the effects of velocity model uncertainty on the wave path from the events to this receiver). Because of the broad disposition of the microseismic monitoring system (see Figure 5.2), the static corrections for different receivers have to be estimated independently for each station. Moreover, the corrections of P- and S-phases at particular sensor can also vary significantly.

Table 5.3: Estimated static corrections.

Station	P correction [ms]	S correction [ms]
OT2	2.9	-2.8
OT1	6.6	-1.6
HAL	3.8	-24.5
STJ	7.3	-11.0
MAT	3.6	-45.0
RI2	-58.0	-122.5

To estimate static corrections, I employed a multi-dimensional optimisation procedure. The target function of optimization was combination of the average RMS location error and the average distance from the hypocenter to the injection interval of the first 200 occurred events. The average location error cannot be the only target since different combinations of static corrections can provide the same average location errors. The reason of the second part of the target function is the assumption that early events should occur in the direct vicinity of the injection interval. The optimization problem was solved by global search. The obtained values of static corrections are given in Table 5.3.

After estimation of the static corrections step (3) of the location procedure was repeated providing the final result (Figure 5.4). Introduction of static corrections does not dramatically change the overall shape of the microseismic cloud, but it shifts the cloud approximately 100 m closer to the injection interval.
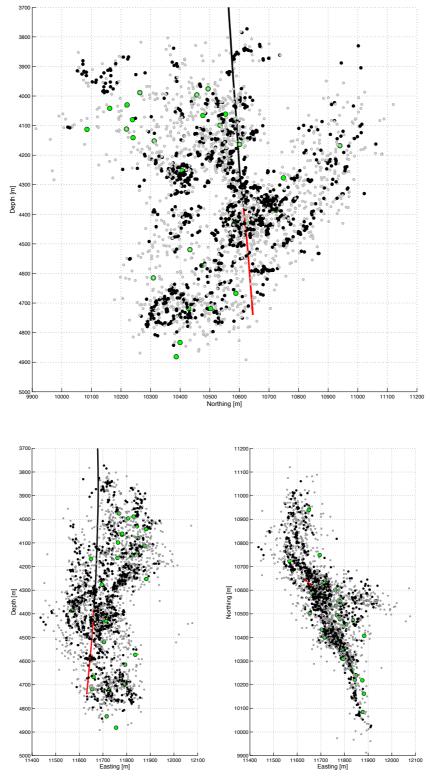
Figure 5.4: Location of 2138 microseismic events. Black line – borehole, red line – open hole section, black dots – clustered events, grey dots – non-clustered events, green dots – events with magnitudes $M_L > 1.7$.

Located microseismic cloud

In total, 2138 microseismic events were located (see Figure 5.4) including 1231 clustered events, which form 260 multiplets. The largest cluster includes 109 events, the smallest includes 3 events. The microseismic cloud has a narrow shape with a main trend oriented in the SSE direction for about 1100 and 1000 m in a vertical plane. In the map view, the cloud splits up into two well pronounced planar nearly vertical structures. The major one has an azimuth of approximately $N156E$, which is close to the orientation of the maximal horizontal stress of $144 \pm 14°$ (Valley & Evans [2006]). The second structure, branches from the main one in the vicinity of the injection interval and propagates in the ESE direction at an azimuth of approximately $N105E$.

There are also less pronounced but noticeable features in the vertical section along the main cloud trend. Multiplets assemble into a system of quasi linear structures, which in the aggregate form a "skeleton" of the cloud, while non-clustered events are sparsely distributed around it.

There is also a number of steeply dipping structures at both sides from the treatment interval with dips of about $60°$. This is consistent with the dominant dips of the natural fractures detected at this interval of the treatment borehole [Häring *et al.*, 2008].

Additionally to the event coordinates, the location procedure also provides statistical characteristics of the obtained results, such as the root-mean-square of residuals at the maximum likelihood hypocenter and the confidence ellipsoids (the confidence ellipsoid represents the 68% confidence region of the located hypocenter for 3 degrees of freedom). In Figure 5.5 one can see error ellipsoids for the first 200 located events after the start of the injection. The average error ellipsoid semi-major axis length for the clustered events is approximately 25 m.

In Figure 5.6 one can see histograms of moment magnitudes and RMS residuals obtained for the clustered and the non-clustered events. The figure shows that multiplets significantly outperform the other events in terms of location residuals. The average misfit for multiplets is about 0.5 ms and approximately 1.5 ms for other events. One might hypothesise that this can be explained by smaller magnitudes of non-clustered events. In this case some events would not be assigned to any cluster because of the lower signal to noise ratio. The magnitude distribution of clustered and non-clustered
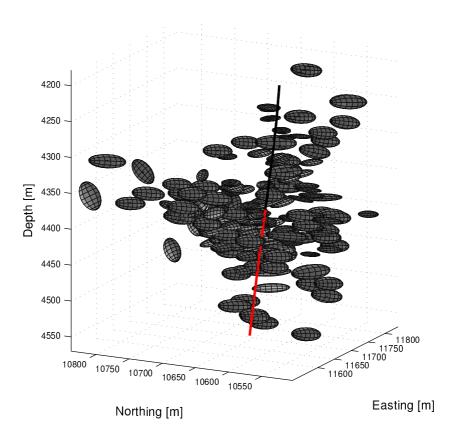
Figure 5.5: 68% confidence error ellipsoids corresponding to first 200 located events.

events, however, shows that it is not the case. Histograms of magnitudes for clustered and non-clustered events are almost identical.

5.4 Microseismic data analysis and processing

The Microseismic Reflection Imaging approach is based on the directional migration method (see Chapter 2 for details), which implies the necessity of polarisation estimation. In order to estimate the polarity of reflected wave it is required that the corresponding wavelet is above the noise level, while in order to locate an event one just has to detect the direct wave arrival times. This makes the imaging approach much more sensitive to the quality of seismic data compared to the applied microseismic event location procedure. Therefore, not all the locatable events are suitable to be taken as
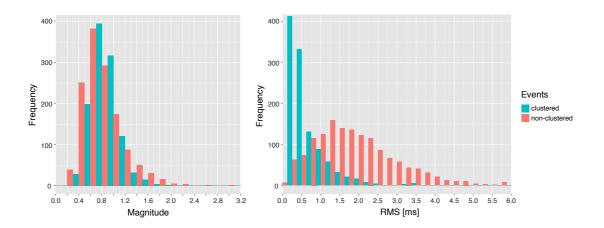
Figure 5.6: Histograms of moment magnitudes (left) and root-mean-square of residuals at maximum likelihood hypocenter (right) for the located clustered and non-clustered events

sources for the imaging procedure. In the following, only the clustered events are used because they are characterised by significantly better locations in terms of RMS misfits and less scattered spatial distribution.

Common-receiver gathers

Here, I consider a recorded seismic trace as suitable for imaging, if it has the signal to noise ratio above some threshold and if the corresponding event has RMS location error below some level. As it was discussed in Chapter 2, in the case of a distributed monitoring system it makes sense to process seismic traces recorded at different sensors independently.

Table 5.4 shows the threshold values used for selection of traces produced by the clustered events and recorded at different receivers. The threshold values for different sensors were selected to sort out unsuitable traces but at the same time to keep a sufficient amount of events to get a consistent image. Small number of traces selected for the OT1 station can be explained by overall low quality of the data recorded by this sensor. In order to get a reference result, the signal to noise threshold for the deepest OT2 sensor is more strict compared to the other stations.

Table 5.4: Event selection parameters for the 6 monitoring stations.

Station	Min SNR	Max Residual [ms]	# of events
OT2	4	4	395
OT1	2	4	206
STJ	2	5	382
HAL	2	4	438
MAT	1	2	353
RI2	2	2	491

Events corresponding to the seismograms selected for the given receivers are shown in Figure 5.7. Selected events locations look quite similar but not identical. The differences can possibly be explained by the impact of the radiation patterns of events and local ambient noise variations at different stations.

To facilitate further processing and imaging, I grouped the selected traces into common-receiver gathers using the algorithm presented in Chapter 2. In Figures 5.8, 5.9 and 5.10 one can see the parts of the produced common-receiver gathers for six considered sensors. The time scale is the same (1.6 sec) for all figures, except of OT2 gather (0.5 sec) which has a much higher frequency content. The P- and S-wave direct wave arrivals are clearly visible in all gathers. It is also noticeable that the considered gathers consist of sets of traces with similar waveforms. Due to the differences of radiation patterns of multiplets one can also see the polarity flips in the direct P-wave. For example, one can see the different signs of P direct wave displacement in traces $71-83$ and $84-100$ in the OT2 gather (Figure 5.8, upper panel).

There are also some coherent waveforms that are not associated with the direct waves. Particularly, at some traces of the OT2 gather (upper panel of Figure 5.8) one can see the well pronounced waveforms recorded at the time between arrival of P- and S-direct waves, which can probably be identified as reflections. This is also the case for other gathers, although the quality of waveforms generally degrades with increasing distance from the stimulated volume.

The seismic data recorded at RI2 sensor (see Figure 5.10, bottom panel) is characterised by a low energy the direct P-wave compared with the gathers for the other sensors. The direct P-wave can be picked because the recorded noise level is relatively
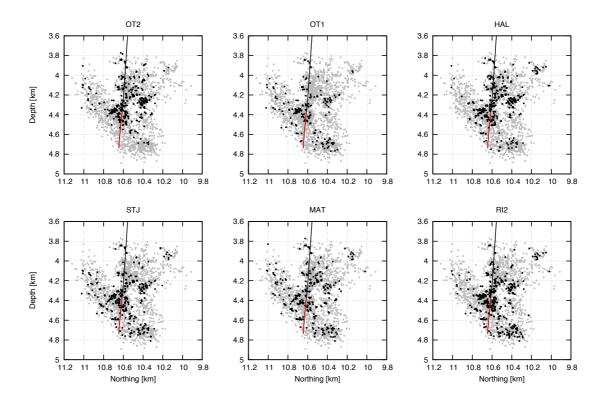
Figure 5.7: Events selected for imaging. Gray dots indicate complete located cloud, black dots indicate selected events for each station.

low, but the energy of this wave is of the same level or even less than energy of the first possible reflection, which can be identified at some traces approximately 100 ms later than the direct wave. I explain this effect by the influence of the radiation pattern of the events.

Transformation of seismograms

The OT2 receiver uses a common configuration of the three axis: two oriented horizontally and the third vertically. All other stations use Galperin configuration (Galperin [1955], Galperin [1985]). In Galperin's system components of the sensors while being mutually orthogonal, are tilted at the same angle (54.7°) to the vertical axis in order to equalise the impact of the gravitational force. The projections of sensor axes to the horizontal plane have angles of 120° between each other.
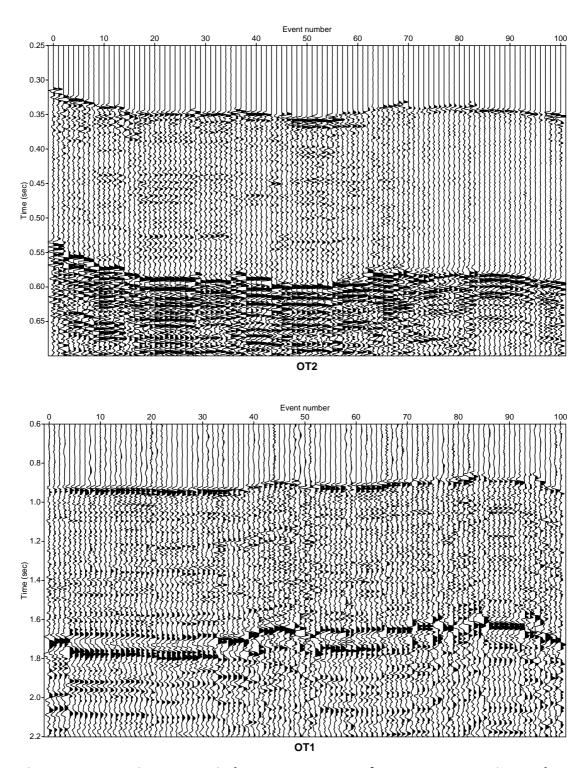
Figure 5.8: Top: First 100 vertical component traces of OT2 common-receiver gather. Bottom: 100 third component traces of OT1 gather.
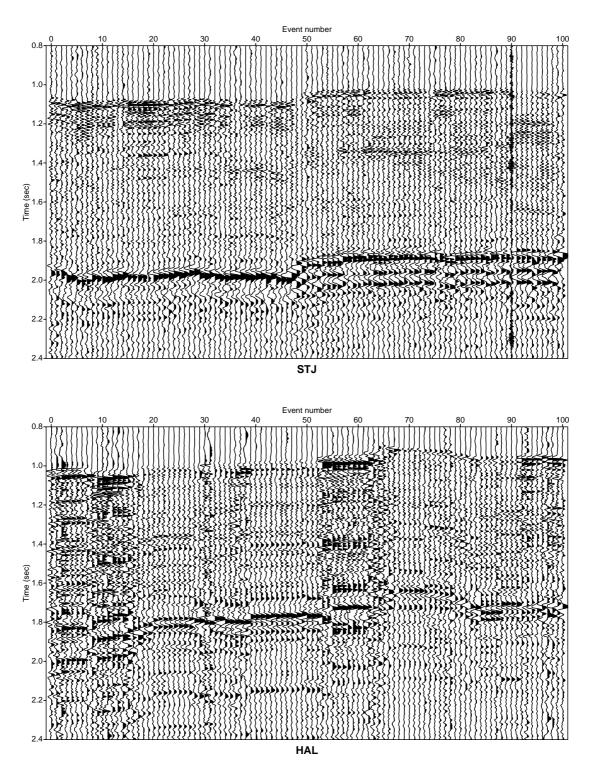
Figure 5.9: 100 third component traces of produced common-receiver gathers for STJ (top) and HAL (bottom) stations.
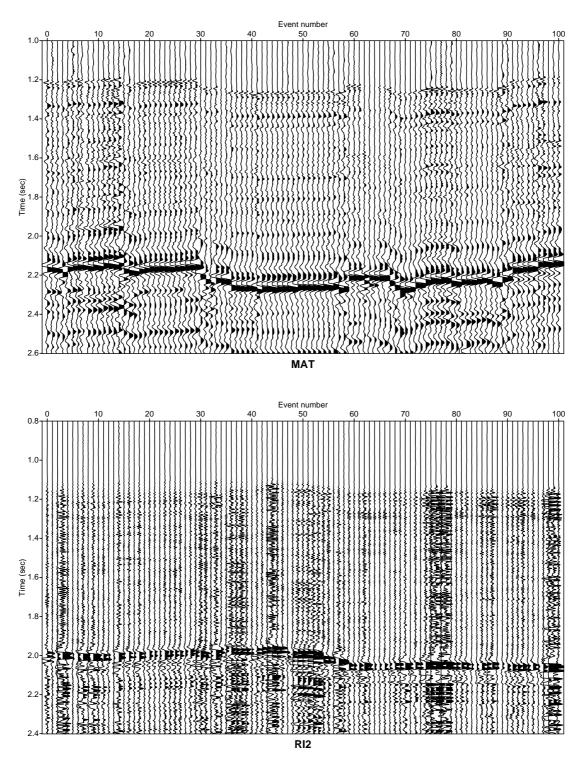
Figure 5.10: 100 third component traces of produced common-receiver gathers for MAT (top) and RI2 (bottom) stations.

The transformation of the response of a seismometer to input ground motion from Galperin UVW system to the conventional XYZ system can be written (Graizer [2009]) as

$$
\begin{pmatrix} X \\ Y \\ Z \end{pmatrix} = \begin{pmatrix} -cos\,\alpha & -cos\,\alpha\;sin\beta & cos\,\alpha\;sin\beta \\ 0 & cos\,\alpha\;cos\beta & -cos\,\alpha\;cos\beta \\ sin\,\alpha & sin\,\alpha & sin\,\alpha \end{pmatrix} \times \begin{pmatrix} U \\ V \\ W \end{pmatrix}
$$

where $\alpha = 35.3°$ is the angle between the axis and the horizontal plane, $\beta = 30°$ is the angle between Y axis and the projection of the V axis onto the horizontal plane. Using this formula I converted the data for all shallow receivers. After this transformation, Z component is defined uniquely for all the sensors, while X and Y have unknown orientation in the horizontal plane. In order to apply directional imaging approach, one has to estimate a polarity vector of incident waves from the recorded seismic data. Therefore, one also needs to estimate the angle between the actual orientation of the sensors and the geographical North-East coordinates.

5.5 Polarisation estimation

In the case of the Basel EGS data, the spatial dimensions of a microseismic cloud are small in respect to the distances from the events to the receivers (see Figure 5.2). Accordingly, the aperture of scattered waves for such system is extremely low in comparison to wide-angle active seismic data. In this situation, the only way to get a resolved image of the cloud interior is to take into account polarity of the reflected waves.

Workflow

The idea of the proposed approach is to apply an optimisation procedure to find the frequency band for which the direct P- and S-waves provide the most accurate polarity estimates and then to use the same filter to estimate polarisation of reflected waves (see Chapter 2 for more details). Microseismic monitoring system of the Basel EGS was installed in the urban area at a relatively shallow depths, therefore one can expect ambient noise conditions to be different at different sensors. Thus, corresponding frequency filters have to be defined independently for different stations. Moreover, frequencies and amplitudes of P- and S-waves also vary significantly (P-waves usually

have higher frequencies and smaller amplitudes, see for example Figure 5.8). Hence, it is useful to construct different filters for P- and S-waves as well. The workflow of polarisation estimation is done for each sensor individually and is described in Chapter 2.

Optimal frequency filters

For each sensor I estimate two band-pass filters estimated independently for P- and S-waves and the notch filter (see Figure 2.5). The results of optimisation are presented in Table 5.5. The slope value for all the filters is constant $S = 5$ Hz.
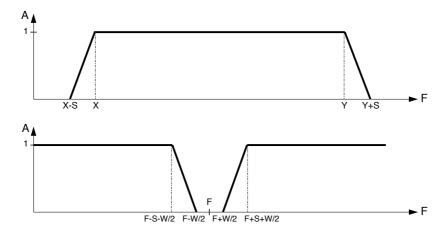
Figure 5.11: Parameters of band-pass and notch frequency filters used for the optimisation.

Table 5.5: Optimal frequency filters.

Station	Band-pass filter [Hz]				Notch filter [Hz]	
	P-wave		S-wave			
	X	Y	X	Y	F	W
OT2	16	87	22	132	55	3
OT1	29	120	6	91	51	3
STJ	19	95	17	122	50	2
HAL	19	128	11	102	50	2
MAT	18	136	—	—	—	—
RI2	—	—	—	—	—	—

The filters were successfully determined for stations OT2, OT1, STJ and HAL. The band-pass filters for P- and S- waves estimated at the same sensor are close to each other but do not coincide. The notch filters for the OT1, STJ and HAL stations are close to each other and clearly represent the standard electronic noise at 50 Hz.

There are two problematic stations that are most distant from the stimulated volume: MAT and RI2. It was not possible to get any reliable polarity estimates for the direct S-wave recorded at the MAT sensor and for both direct P- and S-waves recorded at the RI2 sensor. Hence, the corresponding filters weren't optimised. Introduction of notch filter for the MAT sensor did not make any improvement.

Seismometers azimuthal orientation

During the optimisation procedure, along with optimal filters, azimuthal orientation of the sensors was also determined. It was done using the following algorithm: using the time pick and the waveform data I estimated polarisation of the direct P-wave for each event independently. Then using the source and receiver positions, I estimated theoretical polarisation of the P-wave, which was done for each considered event. Finally, azimuthal correction for each sensor was estimated as a difference between empirical and theoretical polarisation direction averaged over all events.

Table 5.6: Azimuthal orientation of sensors

Station	Azimuth [Deg]
OT2	107.5 ± 0.7
OT1	-170.2 ± 2.3
STJ	-66.7 ± 1.6
HAL	-90.3 ± 1.3
MAT	-130.1 ± 0.9
RI2	—

The results are shown in Table 5.6. The obtained azimuths specify the angles for which the preliminary converted seismic data have to be rotated in the XY plane to coincide with the geographical ENZ system. Positive sign of the angle defines the rotation in counter-clockwise direction. The uncertainties were computed with the assumption of normal distribution of azimuth estimates and 95 % confidence interval. The direct P-
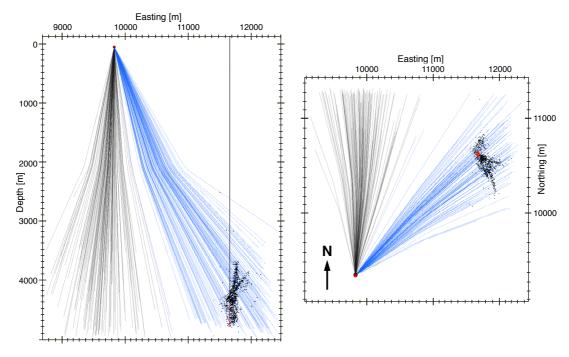
Figure 5.12: Ray trajectories corresponding to the back propagated direct P-wave for the original (black lines) and corrected (blue lines) OT2 sensor orientations.

wave polarity estimates for the data recorded at the RI2 sensor were inconsistent. As a result, the azimuth correction for this sensor was not determined. Ray trajectories corresponding to the back propagated direct P-wave for the original and corrected OT2 sensor orientations are shown in Figure 5.12.

5.6 Migration procedure setup

Imaging volume

The main interest of this study is to get an image of the stimulated reservoir. The targets are the local heterogeneities like fractures and inclusions that may be relatively thin. This implies that the migration grid has to be reasonably fine. The volume that includes all the borehole instruments and the microseismic cloud is about 6.5 x 4 x 5 km. Available technical facilities do not allow to use this volume for imaging with grid spacing suitable for the posed problem. In order to fit into the technical limitations, I

use the cubical volume with 1.5 km edge length centred in the stimulated volume. The corresponding grid has dimensions of 375 x 375 x 375 with the grid cell size of 4 m.

Reflection data

Since there is no a priori geological information about the stimulated reservoir, it is not possible to predict the arrival times of the reflected wave illuminating the target area. In this work I use the following assumption: all the waves arriving between the direct P- and S-waves are treated as PP reflections; waves arriving after the direct S-wave are treated as SS reflections. Obviously, it is a simplification. For instance, PS reflection may arrive earlier than the direct S-wave as well as PP or SP reflections may arrive after the direct S-wave. Nevertheless, the assumption is quite reasonable because it allows one to pre-define the wave type for migration, while the use of the directional migration algorithm in a limited volume helps to reduce the migration artefacts caused by the misinterpretation of wave types. For example, an estimate of the wave propagation direction for S-wave that is treated as P-wave would be orthogonal to the real one. For the case of Basel EGS monitoring system where the distance between receivers and the injection point is much larger than the size of microseismic cloud, such misinterpreted wave will not contribute to the selected imaging volume.

5.7   Imaging results

I applied the imaging procedure to all the microseimsic gathers for which I have estimated the frequency filters (see Table 5.5). As a result, I obtained the PP and SS reflection images from the data recorded at the OT2, OT1, STJ stations and the image of SS reflections for the HAL station. Migration of the HAL PP reflection data and the data recorded at the MAT sensor do not provide any distinct reflectors in the vicinity of the stimulated area. Seismograms recorded at the RI2 station are not migrated because it is not possible to estimate the polarisation with reasonable accuracy.

For the given geometry of acquisition system and the microseismic source locations one can expect that reflected waves recorded at different sensors may illuminate different parts of the reservoir. Therefore location of most reflective areas in images obtained for

various receivers may differ. Assuming that the velocity model and the estimated static corrections are precise, images of PP and SS reflections recorded at the same receiver are expected to reveal generally similar structures. Though the wave path of reflected P- and S- waves can be different and corresponding illuminated areas do not have to necessarily completely coincide. Polarity estimates for P waves are generally significantly more accurate than the estimates for S-waves, so in most cases PP reflection images are more reliable than SS reflections images for the same receiver.

North-South sections

In Figure 5.13 one can see the vertical sections of images obtained from the PP and SS reflections data recorded at OT2 station. The strongest reflector in the PP reflections image is in the southern part of the cloud and has a NNW dip around $45°$. This reflector is accompanied by several weaker reflectors above and below with similar dips. In the northern part of the section there are two SSE dipping reflectors with similar dips of about $60°$ crossing the borehole at depths approximately 4300 m and 4550 m. There is also one nearly horizontal reflector at the bottom part of the reservoir at about 4650 m depth. The SS reflection image section (bottom panel of Figure 5.13) has a smaller amount of reflectors. There is a single strong reflector in the southern part of the image that located in the extension of the strongest reflector in the PP image. Hence, SS reflections seem to illuminate different part of the same structure. In the northern part of the section, there is one reflector that is located close to the deepest reflector in the PP image, but the dip of this reflector is significantly steeper.

The OT2 receiver is much closer to the injection and has much better signal quality in comparison with other stations. Moreover, OT2 is the only considered receiver that was installed in the same geological unit where the stimulated reservoir is located. Therefore, the signals recorded at OT2 are much less affected by uncertainties in the velocity model. Thus, I consider the results for the OT2 sensor as a reference that will be compared to the results for other stations.

The OT1 station imaging results (Figure 5.14) demonstrate a similar distribution of reflectivity. The PP reflections image section reveals the strongest reflector that crosses the borehole at approximately 4550 m depth with dip in the range of $50 - 60°$. This is consistent with the PP imaging results for the data recorded at OT2 (Figure 5.13).

In the southern part of the image there are two parallel reflectors with a dip of about 45°. These reflectors fit almost perfectly with the reflectors in the OT2 PP and OT2 SS images. There is also one horizontal reflector at approximately 4750 m depth, which is about 100 m below the similar reflector in the OT2 PP reflections image. In the SS reflections image section (bottom panel of Figure 5.14) one can see the strongest reflector in the northern part. The bottom part of this reflector is in a good agreement with the corresponding reflector in the PP reflections image, while the upper sub-vertical part is not confirmed by the OT2 images. The sub-horizontal reflector in the bottom part of the OT1 SS image section is deeper than the corresponding reflector in other images. The weaker reflector in the southern part of the OT1 SS image section fits perfectly with the OT1 PP image as well as the OT2 PP image sections.

The STJ images (Figure 5.15) show much less reflectivity compared with the images from OT2 and OT1 sensors. The PP reflection image section contains only two focused reflectors. The first one in the southern part is consistent with the images from OT2 and OT1. The second is in the bottom part of the section. It has dip of around 60° that is similar to the analogous reflectors in the other images, but it is located approximately 200 m deeper. The STJ SS reflection image section is generally similar to the OT2 PP reflections image section. There is the strongest reflector in the southern part. Though it demonstrates slightly higher dip compared to the STJ PP reflections image section, it correlates well with the corresponding reflectors in other images. There is also a number of sub-horizontal reflectors in the bottom part of the STJ SS image section. They correlate well with the corresponding reflectors in the OT2 PP and OT1 PP images. The less pronounced reflector in the northern part of the STJ SS image is quite close by dip and location to the similar reflector in the OT1 SS reflections image section.

The HAL SS reflections image section (Figure 5.16) also shows some reflective areas. Although they generally look similar to the previous images, they seem to be more distorted. Particularly, the reflector in the southern part of the section has a significantly different dip in comparison with other images. The reflectors in the northern part are also slightly shifted in north direction and have deviations in dip.
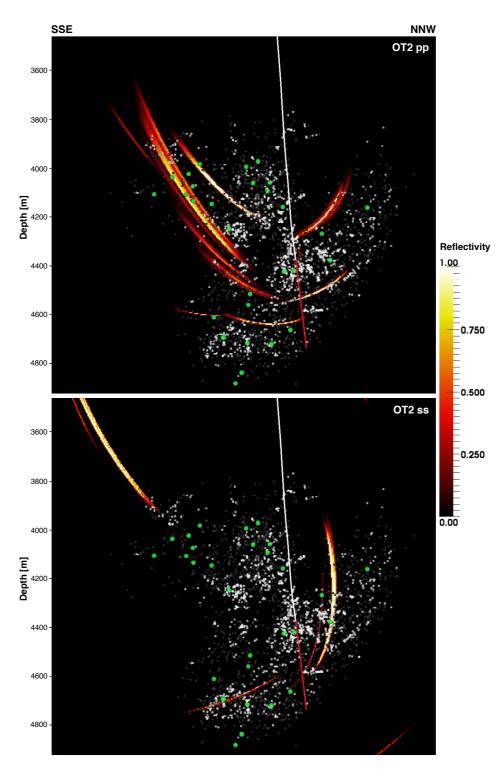
Figure 5.13: Vertical sections of the obtained images for OT2, PP reflections image (top) and SS reflections image (bottom). White solid line – borehole, white dots – clustered events, grey dots – non clustered events, green dots – big events ($M_L > 1.7$), red solid line – borehole open hole section.
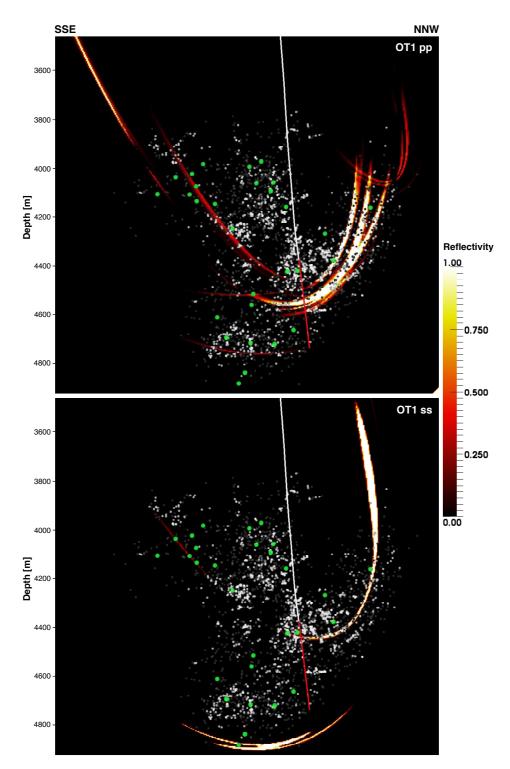
Figure 5.14: Vertical sections of the obtained images for OT1, PP reflections image (top) and SS reflections image (bottom). White solid line – borehole, white dots – clustered events, grey dots – non clustered events, green dots – big events ($M_L > 1.7$), red solid line – borehole open hole section.

Figure 5.15: Vertical sections of the obtained images for STJ, PP reflections image (top) and SS reflections image (bottom). White solid line – borehole, white dots – clustered events, grey dots – non clustered events, green dots – big events ($M_L > 1.7$), red solid line – borehole open hole section.

Figure 5.16: Vertical sections of the obtained images for HAL station SS reflections image. White solid line – borehole, white dots – clustered events, grey dots – non clustered events, green dots – big events ($M_L > 1.7$), red solid line – borehole open hole section.
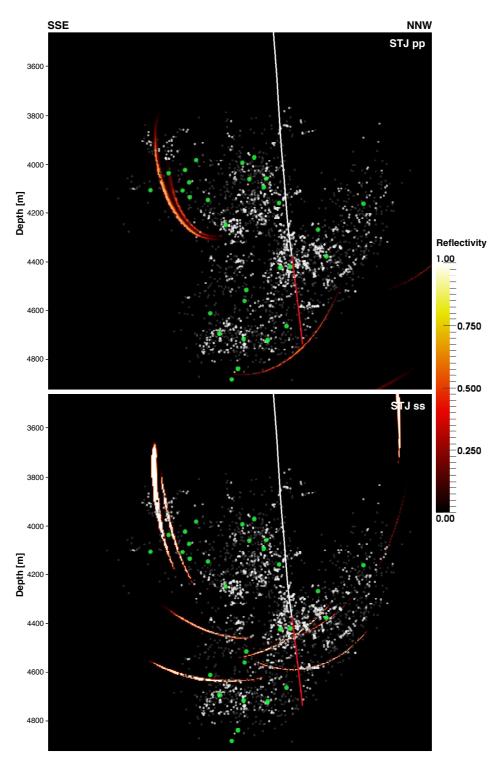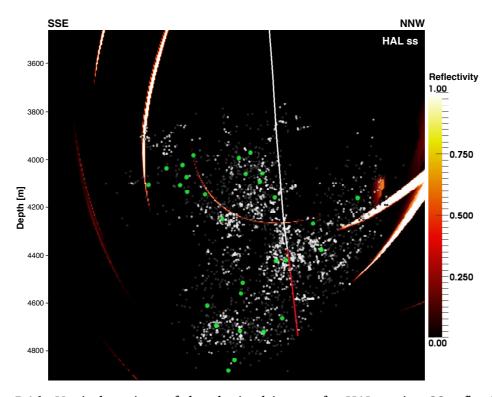
3D representation of the reflectors

An alternative way to present results of imaging is to show reflectors in a form of 3D objects. Since migrated images are 3D grids with reflectivity values in each cell, it is possible to plot the cells with have reflectivity higher than a predefined threshold to show the 3D structure of reflectors.

Figure 5.17 shows 3D iso-surfaces corresponding to the most reflective parts of the OT2 PP and OT1 PP images. To make it more prominent, I plot here only part of 3D reflectors structure belonging to the volume in direct vicinity of the microseismic cloud. The most reflective part of the OT2 PP image, as seen in Figure 5.13 is located in the southern part, while the OT1 PP image has the strongest reflectors in the northern part of the volume (Figure 5.14).
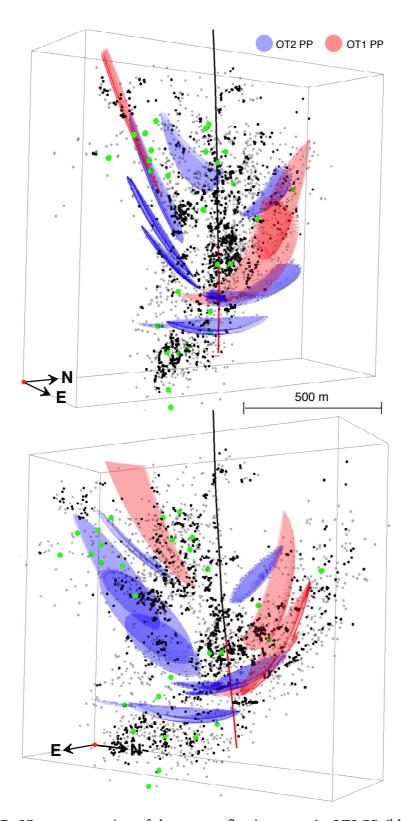
Figure 5.17: 3D representation of the most reflective areas in OT2 PP (blue) and OT1 PP image (red). Black solid line – borehole, black dots – multiple events, grey dots – non clustered events, green dots – big events ($M_L > 1.7$), red solid line – borehole open hole section.

The revealed reflectors have a planar shape. In some cases it is slightly curved because of a limited data aperture. Vertical sections of the images show more details and demonstrate more consistency compared to 3D visualisation. Nevertheless, in the area where most reflective parts are overlapping the reflectors almost coincide by depth and dip.

Altogether the 3D plots of reflectors repeat shape of the seismically active area. There are several sub-parallel structures in the left and right hand side of the volume that coincide with the respective branches of the cloud. There is also a strong horizontal reflector in the bottom part of the reservoir. In the upper part of the cloud any prominent reflectors are not presented. This can be explained by disposition of the sources and receivers. There are not enough microseismic events to illuminate the upper part of the reservoir for the given configuration of seismic sensors.

Consistency of the images

In total, 7 images were obtained using the PP and SS reflection data from 4 borehole sensors. The PP reflections image for the HAL sensor (Figure 5.16) reveals least distinct picture compared with the images from other stations and is not considered further. For the data recorded at OT2, OT1 and STJ sensors I produced focused images for both wave types. These 6 images can be treated as independent results. All microseismic waveforms recorded at different stations were processed individually: for each sensor I have estimated azimuthal orientation and selected its own subset of events suitable for migration. Since the directional migration approach is applied, the PP and SS reflections images obtained for the same receiver do not replicate each other. There are different polarity estimation procedures applied for compressional and shear waves and the thresholds used to select the most reliable parts of the seismic data were defined independently.

A combined plot of vertical North-South sections of the 6 images is shown in Figure 5.18. One can see that, as it was expected, the PP images are more reliable and show more details compared with the SS images. One can also observe that quality of images degrades with increasing distance from the injection point to the receivers (in Figure 5.18 images are sorted by the distance from the receiver to the injection point). Nevertheless, generally all images reveal similar structure of reflectors within and outside of
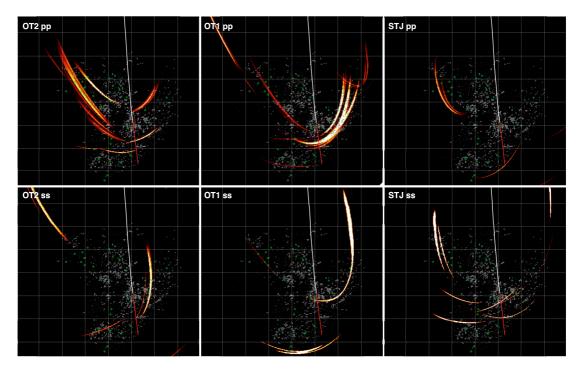
Figure 5.18: Vertical sections of the obtained images for OT2, OT1, STJ sensors (from left to right), for PP and SS reflected waves (top, bottom).

the microseismic cloud. The most of information is contained in the OT2 PP and OT1 PP images. Other images can serve as an independent confirmation of the main results.

5.8 Correlation with borehole data

Highly reflective parts in the obtained images may indicate some local heterogeneities such as inclusions or fault zones. Geological data from the Basel-1 stimulation borehole logs is an independent source of information about such heterogeneities. In Häring *et al.* [2008] it is noted that the bottom part of the well including open hole section is characterised by a natural set of fractures trending NW-SE to NNW-SSE, with steep dips exceeding 60°. Additionally, they identify two fracture zones at 4700 m and 4835 m depth measured along the borehole.

Valley & Evans [2009] investigate the SHmax direction from the observations of wellbore failure derived from the ultrasonic televiewer images obtained in two wells: the
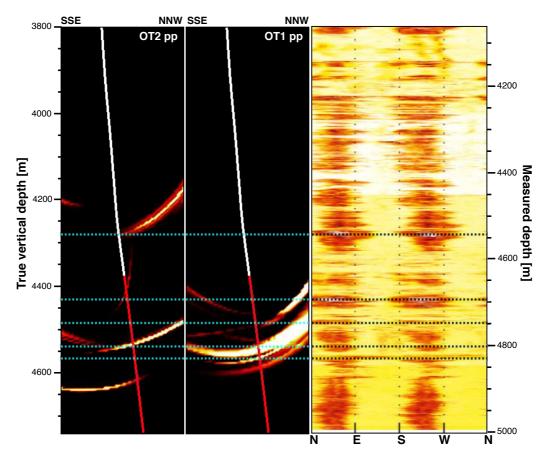
Figure 5.19: Correlation of obtained images and ultrasonic reflectivity acquired in the injection borehole. Left: OT2 PP image vertical section, center: OT1 PP image vertical section, right: acoustic televiewer image by Valley & Evans [2009]. White solid line indicates the geometry of BS1 borehole, red solid line shows the well open hole section. Distance between horizontal and vertical guidelines is 200 m.

exploration well where OT2 sensor was installed and the deep borehole Basel-1 where the injection took place. The borehole was imaged entirely within the granite basement from 2569 m to 4992 m measured depth. The acoustic reflectivity image provides information about the presence of fractures and changes in rock properties.

Figure 5.19 shows the fragments of two most reliable microseimic reflection images (OT2 PP and OT1 PP) in the vicinity of injection well and the bottom part of the ultrasonic reflectivity image for the same well by Valley & Evans [2009]. The upper reflector that intersects the borehole is the reflector from the OT2 PP image, crossing the borehole at 4275 m true vertical depth (TVD) or 4540 m depth measured along

borehole (MD). This depth corresponds to local reflectivity maximum in the televiewer image. The next relatively small reflector at the OT2 PP image crosses the borehole at approximately 4420 m TVD, which is slightly higher than 4430 m TVD (4700 m MD) where a local reflectivity maximum at ultrasonic image is located. This is also consistent with the fault zone at 4700 m MD identified by Häring *et al.* [2008]. The first distinct reflector in the OT1 PP image crosses the borehole at approximately 4470 m TVD (4740 m MD), which corresponds to the area of elevated reflectivity surrounded by a non reflective area on the top and bottom in the televiewer image. The strongest reflector on the both OT2 and OT1 images intersects the well at the interval 4530 – 4570 m TVD (4800 – 4840 m MD), which correlates with the highly reflective areas in the ultrasonic images as well as the fault zone at 4835 m MD mentioned in Häring *et al.* [2008]. Sub-horizontal reflector at 4640 m TVD (4910 m MD) in the OT2 PP image does not coincide with any distinct reflectivity zone, but lays within the highly reflective interval in the bottom part of the borehole in the televiewer image. The ultrasonic reflectivity image also provides information about, direction of the detected heterogeneities. According to Valley & Evans [2009], most of reflectivity is oriented in NE-SW direction (see Figure 5.19). Unfortunately, it is quite complicated to determine the azimuthal direction of reflectors from microseismic images because it is controlled by the geometry of the cloud and the area that can be illuminated.

Generally, the OT2 PP and OT1 PP images are in a good agreement with the televiewer image. Its most reflective parts in the bottom part of the Basel-1 borehole coincide quite well with the reflectors revealed in microseismic reflectivity images. However, there are some high reflectivity areas in the ultrasonic images that are not present in the microseismic images. First, this can be explained by the limitedness of the area that can be illuminated by reflected waves. Second, not all the reflectivity in the televiewer image necessarily has to be heterogeneities penetrating far away from the borehole and therefore might be hardly seen in other images. The obtained images are also confirmed by the two major fault zones in the open hole section identified by Häring *et al.* [2008].

5.9   Correlation with Vp/Vs Ratio Distribution

Kummerow *et al.* [2012] estimate the distribution of Vp/Vs ratio within the Basel
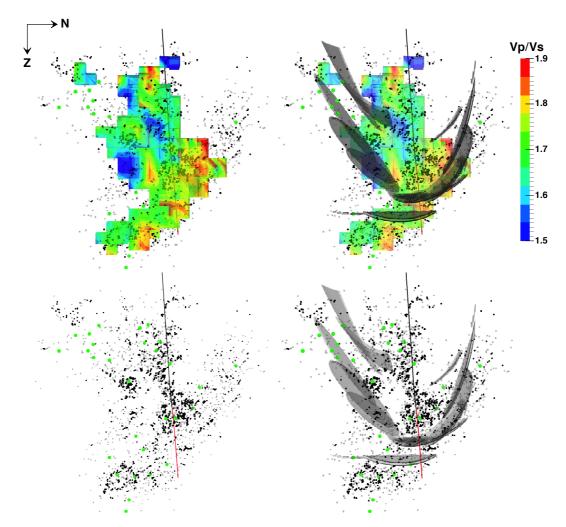
Figure 5.20: Vp/Vs ratio distribution and the strongest reflectors from OT2 PP and OT1 PP images. Black solid line – borehole, black dots – multiple events, grey dots – non clustered events, green dots – big events ($M_L > 1.7$), red solid line – borehole open hole section.

geothermal reservoir from differential arrival time measurements of the microseismic data. The study is based on the same microseismic event locations as I use in this work.

In Figure 5.20 one can see the 3D representation of Vp/Vs ratio distribution and the strongest reflectors from the two most reliable microseismic images (the same as in Figure 5.17, but without colour separation). Estimated Vp/Vs ratio is defined in the 3D grid with cell size of 50 m. In this figure one can see only the cells for which the local Vp/Vs value was determined. The values vary from 1.42 to 2.09 with the average about 1.70, which is close to the Vp/Vs value computed from average reservoir velocities

(1.72).

Though the resolution of the Vp/Vs ratio distribution is relatively low, one can identify several distinct anomaly zones where the ratios are larger or lower than the average. These anomaly zones spatially correlate with the strongest reflectors in the two most reliable microseismic reflection images (OT2 PP and OT1 PP). Particularly, a group of sub-parallel reflectors in the southern part of the image fits to the area where Vp/Vs close to 1.5. In turn, the reflector in the northern part of the region coincides with the area of high Vp/Vs values in the deeper part of the reservoir.

5.10 Discussion

For the interpretation of conventional 3D seismic images, reflectors are used to map large-scale horizons and faults. In this study the illuminated area is substantially restricted and the obtained reflectivity shows local heterogeneities within the stimulated part of the granitic basement. The key question is what kind of geological objects can be imaged using injection induced seismicity and, how the microseismic reflection images can contribute to the reservoir characterisation.

The first possible interpretation is that the reflectors represent fault planes where microseismicity nucleates, but this is in a contradiction with other observations. Particularly, reflectors in the images are flat and have dips less than 60°, while the focal mechanisms of events recorded by the network of the Swiss Seismological Service, which were estimated by Deichmann & Ernst [2009], indicate that the corresponding fault planes are oriented sub-vertically with azimuths close to the principal horizontal stress. It is also confirmed by the overall shape of the cloud that has a planar vertical shape with azimuth of about N150E. There is also one more reason to decline this interpretation. In order to produce any visible reflections, which can be migrated by the imaging procedure, a reflector must have a significant contrast of physical properties in comparison with the background medium. Therefore, the second order cracks produced by simple slip, where most of multiple events are expected to occur (due to their waveform similarity), can unlikely be seen in the image.

On the other hand, independent observations confirm the presence of horizontally oriented heterogeneities in the reservoir. In particular, the vertical projection of the micro-

seismic cloud shows many heterogeneities (see Figure 5.4). In some areas, the events are accumulated, while in others there are no events at all. The borehole logging data analysis also shows some relatively thin horizontally oriented fractures at several depth intervals (see Figure 5.19). Besides, the vertical section of the Vp/Vs ratio distribution also shows significant variations (Figure 5.20).

I analysed the fault plane solutions of multiple events obtained by Rusu [2012]. The author used the same microseismic data as was used in this study to compute earth-quake focal mechanisms for several events in each cluster. He revealed that events from the same cluster, as expected, have quite similar fault plane solutions, and produced cumulative solutions for the 27 biggest clusters. Each solution specifies two possible fault planes that satisfy the data. In order to get one single solution for each cluster I computed the average distance between both planes passing through the centre of the cluster and events form this cluster. The plane that provides the smallest misfit I consider as a fault plane of the cluster. The obtained fault planes as well as the focal mechanisms and the reflectors are shown in Figure 5.21. Each plane is presented in form of a disk. The radius of a disk is the maximal distance between an event and the centre of the cluster. The estimated fault planes are mostly sub-vertical and oriented along the main cloud trend direction. These planes clearly do not coincide with the reflectors, moreover in most cases they intersect or touch the reflectors with an angle close to 90°. A probable interpretation that explains such behaviour is that the imaged reflectors are cracks or weak rock zones with a higher permeability compared to the background rock. These highly permeable zones serve as pathways for the fluid and the elevated fluid pressure to the medium and therefore control the shape of the cloud, which is confirmed by the spatial distribution of microseismicity. The pathways are aseismic, while the majority of microseismicity occurs in the surrounding rock. The clustered events possibly occur in the second order cracks branching from the main pathways. Waveform similarity of events in the clusters can be explained by the fact that they occur at the same or at parallel systems of the second-order fractures. Non-clustered events have a specific source mechanism and can occur as a result of pore pressure perturbation in the background rock.

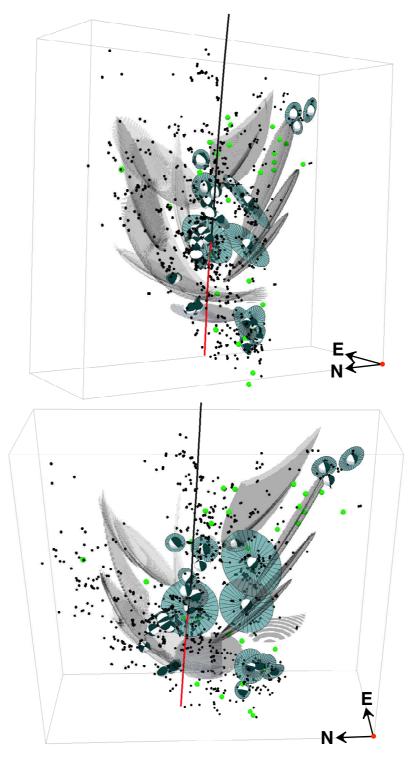Figure 5.21: Focal mechanisms of 27 biggest clusters and the corresponding fault planes (cyan disks); combined 3D representation of the most reflective areas in the OT2 PP and OT1 PP images (grey planar structures). Black solid line – borehole, black dots – multiple events, green dots – big events, red solid line – borehole open hole section, grey box – the volume in which reflectors are plotted.

5.11   Conclusion

This chapter focused on the application of the Microseismic Reflection Imaging method to the Basel EGS data. Having restricted acquisition, considered dataset includes much more high quality microseismic events compared to the data presented in the previous two chapters. It allowed me to demonstrate the potential of the method for rich microseismic datasets. The obtained images mapped consistent network of reflectors in the vicinity of the injection interval, inside the microseismic cloud.

Compared to the results from the previous two chapters, the image of the Basel EGS stimulated volume is much more distinct. It is detailed enough to speculate on possible nature of the observed reflectivity. Interpretation of the reflectors within the stimulated reservoir as fluid filled cracks may suggest the possible practical application of the method which will be discussed in the last chapter.

Conclusions and outlook

The aim of this work has been to develop a methodology that would allow the use of waveforms from microseismic events in reflection imaging. This methodology included the workflow for microseismic data processing and the set of algorithms for further migration. The method was intended to image the internal structure of a seismically active zone. In contrast to conventional active seismic, microseismic reflection data have a number of distinctive characteristics, for example, the location of sources directly inside the area of interest, a limited data aperture and high frequency signals. On the one hand, this makes the application of conventional migration techniques quite problematic. On the other hand, because of these characteristics the microseismic reflection data may contain independent information about the fine structure of the relatively small volume in the vicinity of a microseismic cloud. In short, the purpose of this thesis has been to understand whether there is such information in microseismic data and, if so, to find out how to extract it.

In order to identify possible reflections in microseismic data, I proposed an algorithm that specifies how the recordings from individual events can be grouped together. The idea behind this approach is to consider the data recorded at different receivers independently. In addition to this, all the traces with microseismic waveforms should be shifted in such a way that zero time on each trace corresponds to the origin time of the respective event. Next, the seismic traces are sorted in such a way that adjacent traces correspond to the events located in close proximity to each other. Finally, all the sorted traces are assembled into a gather. A common receiver gather constructed in this way helps to evaluate the presence of reflection data. The assumption behind this is as follows: if the seismic trace from one event includes a reflected wave, then the seismic traces from other closely located events will also include reflected waves arriv-

ing at approximately the same time. Thus, the criterion of the presence of reflection in the microseismic data is the presence of coherent arrivals in a gather. To accommodate the unique features of microseismic data, I suggested a method that includes a data processing workflow and imaging scheme. The method identifies and uses for further imaging only the most reliable parts of the reflection data. This is done in order to avoid image distortion caused by source location uncertainties and a low signal to noise ratio. For the imaging I employed the Fresnel Volume Migration algorithm due to its capability in reducing migration artefacts originating from the low aperture of the data.

The suggested method was applied to three different microseismic datasets including both natural and induced seismicity with various data quality and acquisition geometries. The first dataset is the natural seismicity data acquired at the San Andreas Observatory at Depth, United States. It represents the case where a few events were recorded by a relatively large amount of receivers. I considered six microearthquakes recorded by the 80 level receiver array. The microseismic reflection data were migrated and revealed a well-resolved image of the fault branch vicinity near the monitoring well. The revealed reflectors are consistent with the borehole lithology and the existing active seismic reflection images. Another dataset that was considered was the induced seismicity data from the German Continental Deep Drilling Program (KTB). This dataset is characterised by relatively poor data quality and extremely restricted acquisition. It includes 50 microseismic events recorded at the single borehole receiver. Since the unreliable part of the reflection the data was automatically excluded, only a small part of the data contributed to the final result. Consequently, the obtained image covered only a small volume in the vicinity of the microseismic cloud. However, the imaged reflector is in agreement with the large scale fault zone image obtained by active seismic profiling. The third example illustrated how the method works in the case evolving a large amount of high quality data. The dataset considered was acquired during the stimulation of the enhanced geothermal system in Basel, Switzerland. The data include more than 2000 microseismic events recorded at five shallow and downhole sensors installed at different boreholes and at different distances from the injection point, providing quite good spatial coverage. The obtained images revealed the distinct network of the reflectors in the vicinity of the injection interval, inside the microseismic cloud. These findings correlate well with the borehole ultrasonic imager data.

There are a number of existing studies that have attempted to use microseismic wave-

form data for the reflection imaging. Some authors apply conventional migration algorithms to microseismic data. The results are somewhat questionable, since the standard migration techniques do not take into account the specific features of microseismic data. The Acoustic Emission method dedicated to work with microseismic reflection data is in some cases able to resolve large-scale geological structures near the microseismic cloud, though it is not suitable for the imaging of objects located within the direct vicinity of seismicity. In light of the existing studies, the Microseismic Reflection Imaging approach demonstrates the ability to significantly reduce the migration artefacts caused by the relatively low energy and limited aperture of microseismic data. To the best of my knowledge, the presented method is the only one which is capable to resolve the area inside the seismically active zone and constructing a high resolution image of its local heterogeneities.

The Microseismic Reflection Imaging method cannot be considered a universal tool. The main limiting factor derives from the uncontrolled nature of microseismic sources. Without the possibility of placing a source at a certain position one cannot guarantee that a particular area of the subsurface will be illuminated. This implies that in the general case, microseismic reflection data cannot cover area of interest completely. Another factor that limits the applicability of the method is the low energy of microseismic events in comparison with active seismic sources. In order to estimate wavefield polarity, which is necessary for the imaging algorithm, the useful signal should be substantially stronger than the noise. This limitation makes the application of the method to the data acquired from the surface almost impossible.

Microseismic reflection imaging can provide a high resolution image of the inner part of a seismically active zone. Since the energy and spatial coverage of sources is limited, the method is unlikely to be useful for the imaging of large-scale geological objects. Instead, it allows one to look inside a seismically active zone. In addition to microseismic source locations, microseismic reflection data can be used as an independent source of information about pre-existing faults. Chapter 5 shows that in the case of a rich dataset, the Microseismic Reflection Imaging method can also image relatively weak reflectors, which were interpreted as fluid-filled cracks inside the stimulated zone. This indicates that the method can be used as a tool for the characterisation of a stimulated reservoir. For example, the method can be helpful in monitoring the stimulated volume, preventing possible drainage related to pre-existing fractures, and helping to find an efficient position for injection or extraction wells.
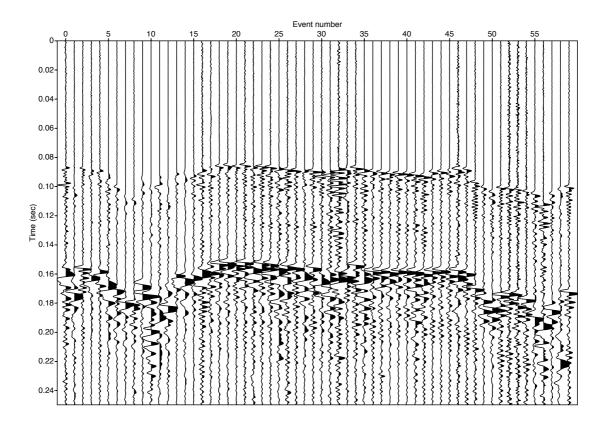
Figure 6.1: Common receiver gather constructed from hydraulic fracturing-induced seismicity data.

Another possible application of the method is the near-real time monitoring of reservoir stimulation[1]. Before the migration, one needs to perform several preparatory steps such as frequency filter optimisation and the specification of the imaging volume. To do this, it is enough to use the first few hundreds events. The reflection data from the events induced later can be migrated using predefined parameters. Each event can be migrated independently and used for the gradual updating of the final image. The computation time necessary for the migration of one event is insignificant for the modern computation facilities. As such, the method allows to get a constantly updated image of a reservoir during the stimulation.

There are several aspects of microseismic reflection imaging that have not been covered in this work. One of them is the "decoupling" of the microseismic waveform data. In contrast to standard active seismic sources, microseismic sources have rather complex

---

[1]In this case a near-real time microseismicity location algorithm would be necessary.

radiation patterns. For this reason in this work I have used the absolute values of signal amplitudes for the image stacking. Alternatively, this problem can be solved more efficiently. If the focal mechanisms of events are determined, theoretically it is possible to use this information for the "decoupling" of microseismic waveforms. In other words, one could reduce the impact of a complex radiation pattern to microseismic recordings and transform it into a form similar to the active seismic data. The benefit of such a transformation would be the possibility of stacking the signal amplitudes taking into account its sign. It would further improve the imaging resolution and help to resolve more of the features in the microseismic reflection images. However, this problem demands additional theoretical and experimental considerations.

A second possible further research direction could be the application of the Microseismic Reflection Imaging approach to hydraulic fracturing data. Currently, hydraulic fracturing induced seismicity is a highly relevant topic and new methods for its processing are of great interest. Unfortunately, the hydraulic fracturing induced seismicity data only became available to me when this thesis was almost complete. For this reason, it was not considered here. However, I did perform a preliminary analysis of a hydraulic fracturing dataset and constructed the common receiver gather using the existing microseismic event locations. In Figure 6.1 one can see a part of this gather. The figure shows some arrivals that may be related to reflections[1]. With some modifications the Microseismic Reflection Imaging approach can be applied to this type of data. However, this task could be rather challenging, since hydraulic fracturing induced seismicity is characterised by extremely low magnitudes and usually located in shale which is highly anisotropic.

I hope that the ideas and the method presented in this thesis will have an impact on the way microseismic data are used. The application examples show that instead of just being a side product of reservoir treatment, microseismic waveforms can provide a unique insight into what is going on in a reservoir and enable the observation of the features of a seismically active zone that are not detectable by other methods.

---

[1]Here I mean the coherent event at approximately 120 ms time from events # 25 – 40 which unlikely can be attributed to direct P- or S-waves. Another example is the arrival at approximately 195 ms recorded from traces # 20 – 35, which arrives after S-wave first arrival and can be attributed to second S-direct wave appeared due to the velocity anisotropy in shales or a reflected wave.

REFERENCES

ASANUMA, H., TAMAKWA, K., NIITSUMA, H., BARIA, R. & HÄRING, M. (2011a). Reflection imaging of EGS reservoirs at Soultz and Basel using microseismic multiplets as a source. In *GRC Transactions, Geothermal Resources Council*, vol. 35, 295–299, Geothermal Resources Council, Davis, California. 58, 59

ASANUMA, H., TAMAKWA, K., SOMA, N., NIITSUMA, H., BARIA, R. & HÄRING, M. (2011b). Reflection imaging of EGS reservoirs using microseismicity as a source. In *Thirty-Sixth Workshop on Geothermal Reservoir Engineering*, Stanford University, Stanford, California. 7

BACHMANN, C.E., WIEMER, S., WOESSNER, J. & HAINZL, S. (2011). Statistical analysis of the induced Basel 2006 earthquake sequence: introducing a probability-based monitoring approach for Enhanced Geothermal Systems. *Geophysical Journal International.* 59

BAISCH, S., BOHNHOFF, M., CERANNA, L., TU, Y. & HARJES, H.P. (2002). Probing the crust to 9-km depth: fluid-injection experiments and induced seismicity at the KTB superdeep drilling hole, Germany. *Bulletin of the Seismological Society of America*, **92**, 2369–2380. 44

BEDNAR, J.B. (2005). A brief history of seismic migration. *Geophysics*, **70**, 3MJ–20MJ. 5

BIONDI, B. (2006). *3D seismic imaging.* 14, Society of Exploration Geophysicists. 18, 19

BLEIBINHAUS, F., HOLE, J.A., RYBERG, T. & FUIS, G.S. (2007). Structure of the california coast ranges and san andreas fault at safod from seismic waveform inversion and reflection imaging. *J. Geophys. Res.*, **112**, doi:10.1029/2006JB004611. 28, 36, 38

Boness, N. & Zoback, M. (2006). A multi-scale study of the mechanisms controlling shear velocity anisotropy in the san andreas fault observatory at depth. *Geophysics*, **71**, F131–F136, doi:10.1190/1.2231107. 39

Bormann, P. (2002). *IASPEI: New Manual of Seismological Observatory Practice (NM-SOP)*. GeoForschungsZentrum. 22

Bradbury, K., Barton, D., Solum, J., Draper, S. & Evans, J.P. (2007). Mineralogic and textural analyses of drill cuttings from the San Andreas Fault Observatory at Depth (SAFOD) boreholes: Initial interpretations of fault zone composition and constraints on geologic models. *Geosphere*, **3**, 299–318. 29

Buske, S. (1999). 3-D prestack Kirchhoff migration of the ISO89-3D data set. In *Seismic Exploration of the Deep Continental Crust*, 157–171, Springer. 53

Buske, S., Gutjahr, S., Rentsch, S. & Shapiro, S. (2007). Application of fresnel-volume-migration to the safod2003 data set. *EAGE 69th annual meeting and technical exhibition, London, Expanded Abstracts*, **P335**. 28, 36, 38

Buske, S., Gutjahr, S. & Sick, C. (2009). Fresnel volume migration of single-component seismic data. *Geophysics*, **74**, WCA47–WCA55. 8, 18, 20

Ĉervený, V. (2001). *Seismic Ray Theory*. 20, 32

Cervenỳ, V. & Soares, J.E.P. (1992). Fresnel volume ray tracing. *Geophysics*, **57**, 902–915. 20

Chavarria, J.A., Malin, P., Catchings, R.D. & Shalev, E. (2003). A look inside the san andreas fault at parkfield through vertical seismic profiling. *Science*, **302**, 1746–1748. 3, 9, 27, 36, 38

Chavarria, J.A., Goertz, A., Karrenbach, M., Paulsson, B., Milligan, P., Soutyrine, V., Hardin, A., Dushman, D. & LaFlame, L. (2007). The use of vsp techniques for fault zone characterization: An example from the san andreas fault. *The Leading Edge*, **26**, 770–776. 27, 29

Courboulex, F., Larroque, C., Deschamps, A., Gélis, C., Charreau, J. & Stéphan, J.F. (2003). An unknown active fault revealed by microseismicity in the south-east of France. *Geophysical Research Letters*, **30**. 2

DAMEN, K., FAAIJ, A. & TURKENBURG, W. (2003). Health, safety and environmental risks of underground CO2 sequestration. *Copernicus Institute for Sustainable Development and Innovation, Países Bajos.* 1

DANESHFAR, B. & BENN, K. (2002). Spatial relationships between natural seismicity and faults, southeastern Ontario and north-central New York state. *Tectonophysics,* **353**, 31–44. 2

DEICHMANN, N. & ERNST, J. (2009). Earthquake focal mechanisms of the induced seismicity in 2006 and 2007 below Basel (Switzerland). *Swiss Journal of Geosciences,* **102**, 457–466, 10.1007/s00015-009-1336-y. 58, 93

DYER, B.C., SCHANZ, U., LADNER, F., HÄRING, M.O. & SPILLMAN, T. (2008). Microseismic imaging of a geothermal reservoir stimulation. *The Leading Edge,* **27**, 856–869. 3, 9, 58, 60, 65

ECONOMIDES, M. & NOLTE, K. (2000). *Reservoir stimulation.* John Wiley & Sons. 57

EMMERMANN, R. & LAUTERJUNG, J. (1997). The German continental deep drilling program KTB: overview and major results. *Journal of Geophysical Research,* **102**, 18179–18. 44

GALPERIN, E.I. (1955). Azimuthal method of seismic observations (in Russian). *Gostoptechizdat,* **80**. 63, 72

GALPERIN, E.I. (1985). *Vertical seismic profiling and its exploration potential.* Reidel Publishing, Dordrecht. 63, 72

GIARDINI, D. (2009). Geothermal quake risks must be faced. *Nature,* **462**, 848–849. 1, 58

GRAIZER, V. (2009). The Response to Complex Ground Motions of Seismometers with Galperin Sensor Configuration. *Bulletin of the Seismological Society of America,* **99**, 1366–1377. 76

GRÄSLE, W., KESSELS, W., KÜMPEL, H.J. & LI, X. (2006). Hydraulic observations from a 1 year fluid production test in the 4000 m deep KTB pilot borehole. *Geofluids,* **6**, 8–23. 44, 45

HANEY, F., KUMMEROW, J., LANGENBRUCH, C., DINSKE, C., SHAPIRO, S.A. & SCHERBAUM, F. (2011). Magnitude estimation for microseismicity induced during the ktb 2004/2005 injection experiment. *Geophysics,* **76**, WC47–WC53. 47

HARDEBECK, J.L. & SHEARER, P.M. (2002). A new method for determining first-motion focal mechanisms. *Bulletin of the Seismological Society of America*, **92**, 2264–2276. 23

HÄRING, M., SCHANZ, U., LADNER, F. & DYER, B. (2008). Characterisation of the Basel 1 enhanced geothermal system. *Geothermics*, **37**, 469–495. 58, 59, 60, 61, 68, 89, 91

HARJES, H.P., BRAM, K., DÜRBAUM, H.J., GEBRANDE, H., HIRSCHMANN, G., JANIK, M., KLÖCKNER, M., LÜSCHEN, E., RABBEL, W., SIMON, M. *et al.* (1997). Origin and nature of crystal reflections: Results from integrated seismic measurements at the KTB superdeep drilling site. *Journal of Geophysical Research: Solid Earth (1978– 2012)*, **102**, 18267–18288. 44

HICKMAN, S., ZOBACK, M., YOUNKER, L. & ELLSWORTH, W. (1994). Deep scientific drilling in the san andreas fault zone. *Eos, Transactions American Geophysical Union*, **75**, 137–142. 28

HIRSCHMANN, G. (1996). KTB – The structure of a Variscan terrane boundary: seismic investigation – drilling – models. *Tectonophysics*, **264**, 327–339. 44

HOLDITCH, S.A. (2003). The increasing role of unconventional reservoirs in the future of the oil and gas business. *Journal of petroleum technology*, **55**, 34–37. 1, 57

JAYA, M.S., BUSKE, S., KUMMEROW, J., RESHETNIKOV, A. & SHAPIRO, S.A. (2009). Seismic Attribute Analysis of the 3-D Depth-migrated Image and Its Correlation With the Induced Microseismicity. In *EAGE 71st Conference and Technical Exhibition*. 53

JURKEVICS, A. (1988). Polarization analysis of three-component array data. *Bulletin of the Seismological Society of America*, **78**, 1725–1743. 12, 32

KANASEWICH, E.R. (1981). *Time sequence analysis in geophysics*. 32

KUMMEROW, J. (2010). Using the value of the crosscorrelation coefficient to locate microseismic events. *Geophysics*, **75**, MA47–MA52. 47, 65

KUMMEROW, J. & SHAPIRO, S. (2010). Microseismic Event Relocation Using Arrival Times and Cross-correlation Coefficients - A Synthetic Study. Expanded abstracts, EAGE 72nd annual meeting and technical exhibition, Barcelona. 65

KUMMEROW, J., SHAPIRO, S., ASCH, G., DINSKE, C. & ROTHERT, E. (2006a). Interpretation of fluid-induced microseismicity at 4km depth at the German Deep Drilling Site (KTB). In *EAGE 68th Conference and Technical Exhibition*, D013. 47

KUMMEROW, J., SHAPIRO, S., DINSKE, C. & ASCH, G. (2006b). Injection-Induced Microseismicity at the German Deep Drilling Site (KTB) at 4km Depth. In *AGU Fall Meeting Abstracts*, vol. 1. 47

KUMMEROW, J., SHAPIRO, S., ASANUMA, H. & HÄRING, M. (2011). Application of an Arrival Time and Cross Correlation Value-based Location Algorithm to the Basel 1 microseismic Data. Expanded abstracts, EAGE 73th annual meeting and technical exhibition, Vienna. 65

KUMMEROW, J., A. RESHETNIKOV, M.H. & ASANUMA, H. (2012). Distribution of the Vp/Vs Ratio within the Basel 1 Geothermal Reservoir from Microseismic Data. Expanded abstracts, EAGE 74th annual meeting and technical exhibition, Copenhagen. 65, 91

LOMAX, A., VIRIEUX, J., VOLANT, P. & BERGE, C. (2000). Probabilistic earthquake location in 3D and layered models: Introduction of a metropolis-gibbs method and comparison with linear locations. In C. Thurber & N. Rabinowitz, eds., *Advances in Seismic Event Location*, 101–134, Springer. 47, 65

LÜTH, S., BUSKE, S., GÖRTZ, A. & GIESE, R. (2005). Fresnel-volume-migration of multicomponent data. *Geophysics*, **70**, S121–S129. 8, 18, 20

MACKENZIE, J.J. (1998). Oil as a finite resource. *Nonrenewable resources*, **7**, 97–100. 1

MAJER, E.L., BARIA, R., STARK, M., OATES, S., BOMMER, J., SMITH, B. & ASANUMA, H. (2007). Induced seismicity associated with enhanced geothermal systems. *Geothermics*, **36**, 185–222. 1

MAXWELL, S.C., RUTLEDGE, J., JONES, R. & FEHLER, M. (2010). Petroleum reservoir characterization using downhole microseismic monitoring. *Geophysics*, **75**, 75A129–75A137. 2

MAYERHOFER, M., LOLON, E., WARPINSKI, N., CIPOLLA, C., WALSER, D. & RIGHTMIRE, C. (2008). What is stimulated rock volume? In *SPE Shale Gas Production Conference*. 2

MUÑOZ, D., CISTERNAS, A., UDIAS, A., MEZCUA, J., SANZ DE GALDEANO, C., MORALES, J., SÁNCHEZ-VENERO, M., HAESSLER, H., IBAÑEZ, J. & BUFORN, E. (2002). Microseismicity and tectonics in the Granada Basin (Spain). *Tectonophysics*, **356**, 233–252. 2

Nadeau, R.M., Michelini, A., Uhrhammer, R.A., Dolenc, D. & McEvilly, T.V. (2004). Detailed kinematics, structure and recurrence of micro-seismicity in the SAFOD target region. *Geophysical Research Letters*, **31**. 29

Nur, A. & Booker, J.R. (1972). Aftershocks caused by pore fluid flow? *Science*, **175**, 885–887. 57

Over, J., De Vries, J. & Stork, J. (1999). *Removal of CO2 by Storage in the Deep Underground, Chemical Utilization and Biofixation: Options for the Netherlands*. Novem. 1

Paulsson, B.N. & Toro, F.C. (2002). A Quantum Leap in Borehole Seismic Imaging. *GAS TIPS*, **8**, 28–31. 27

Plenefisch, T. & Bonjer, K. (1997). The stress field in the Rhine Graben area inferred from earthquake focal mechanisms and estimation of frictional parameters. *Tectonophysics*, **275**, 71–97. 60

Podvin, P. & Lecomte, I. (1991). Finite difference computation of traveltimes in very contrasted velocity models: a massively parallel approach and its associated tools. *Geophysical Journal International*, **105**, 271–284. 24

Rentsch, S., Buske, S., Lüth, S. & Shapiro, S.A. (2007). Fast location of seismicity: A migration-type approach with application to hydraulic-fracturing data. *Geophysics*, **72**, S33–S40. 30, 32

Rentsch, S., Buske, S., Gutjahr, S., Kummerow, J. & Shapiro, S.A. (2010). Migration-based location of seismicity recorded with an array installed in the main hole of the San Andreas Fault Observatory at Depth (SAFOD). *Geophysical Journal International*, **182**, 477–492. 32

Reshetnikov, A., Kummerow, J., Shapiro, S., Asanuma, H. & Häring, M. (2011). Using Microseismicity to Image the Structure of the Basel Geothermal Reservoir. Expanded abstracts, EAGE 73th annual meeting and technical exhibition, Barcelona. 59

Ripperger, J., Kästli, P., Fäh, D. & Giardini, D. (2009). Ground motion and macroseismic intensities of a seismic event related to geothermal reservoir stimulation below the city of Basel—observations and modelling. *Geophysical Journal International*, **179**, 1757–1771. 57

ROTHERT, E. & SHAPIRO, S.A. (2007). Statistics of fracture strength and fluid-induced microseismicity. *Journal of Geophysical Research: Solid Earth (1978–2012)*, **112**. 2

RUSU, A. (2012). Processing of microseismic data for imaging the Basel geothermal reservoir - Bachelor's thesis, Fachrichtung Geophysik, Freie Universität Berlin, Germany. 94

RUTLEDGE, J., PHILLIPS, W. & MAYERHOFER, M. (2004). Faulting induced by forced fluid injection and fluid flow forced by faulting: An interpretation of hydraulic-fracture microseismicity, Carthage Cotton Valley gas field, Texas. *Bulletin of the Seismological Society of America*, **94**, 1817–1830. 2

SAMSON, J.C. (1977). Matrix and stokes vector representations of detectors for polarized waveforms: theory, with some applications to teleseismic waves. *Geophysical Journal of the Royal Astronomical Society*, **51**, 583–603. 6, 14

SANFORD, A., ALPTEKIN, Ö. & TOPPOZADA, T. (1973). Use of reflection phases on microearthquake seismograms to map an unusual discontinuity beneath the Rio Grande rift. *Bulletin of the Seismological Society of America*, **63**, 2021–2034. 6

SCALES, J.A. (1995). *Theory of seismic imaging*. Springer-Verlag. 2

SCHLEICHER, J., TYGEL, M. & HUBRAL, P. (1993). 3-d true-amplitude finite-offset migration. *Geophysics*, **58**, 1112–1126. 18, 23

SCHLEICHER, J., TYGEL, M. & HUBRAL, P. (2007). *Seismic true-amplitude imaging*. Society of Exploration Geophysicists, The International Society of Applied Geophysics. 2

SCHNEIDER, W.A. (1978). Integral formulation for migration in two and three dimensions. *Geophysics*, **43**, 49–76. 18

SCHORLEMMER, D. & WIEMER, S. (2005). Microseismicity data forecast rupture area. *Nature*, **434**, 1086. 27

SHAPIRO, S., KUMMEROW, J., DINSKE, C., ASCH, G., ROTHERT, E., ERZINGER, J., KÜMPEL, H. & KIND, R. (2006). Fluid induced seismicity guided by a continental fault: Injection experiment of 2004/2005 at the German Continental Deep Drilling Site (KTB). *Geophys. Res. Lett.*, **33**, doi:10.1029/2005GL024659. 45

SHAPIRO, S.A., HUENGES, E. & BORM, G. (1997). Estimating the crust permeability from fluid-injection-induced seismic emission at the ktb site. *Geophysical Journal International*, **131**, F15–F18. 2

SHAPIRO, S.A., AUDIGANE, P. & ROYER, J.J. (1999). Large-scale in situ permeability tensor of rocks from induced microseismicity. *Geophysical Journal International*, **137**, 207–213. 2

SHAPIRO, S.A., ROTHERT, E., RATH, V. & RINDSCHWENTNER, J. (2002). Characterization of fluid transport properties of reservoirs using induced microseismicity. *Geophysics*, **67**, 212–220. 2

SHAPIRO, S.A., PATZIG, R., ROTHERT, E. & RINDSCHWENTNER, J. (2003). Triggering of seismicity by pore-pressure perturbations: Permeability-related signatures of the phenomenon. *Pure and Applied Geophysics*, **160**, 1051–1066. 1

SHAPIRO, S.A., RENTSCH, S. & ROTHERT, E. (2005). Characterization of hydraulic properties of rocks using probability of fluid-induced microearthquakes. *Geophysics*, **70**, F27–F34, doi:10.1190/1.1897030. 53, 57

SHAPIRO, S.A., DINSKE, C., LANGENBRUCH, C. & WENZEL, F. (2010). Seismogenic index and magnitude probability of earthquakes induced during reservoir fluid stimulations. *The Leading Edge*, **29**, 304–309. 57

SHEARER, P.M. (1997). Improving local earthquake locations using the L1 norm and waveform cross correlation: Application to the Whittier Narrows, California, aftershock sequence. *Journal of Geophysical Research*, **102**, 8269–8283. 47

SOMA, H., NIITSUMA, H. & BARIA, R. (1997). Estimation of deeper structure at the Soultz Hot Dry Rock field by means of reflection method using 3c ae as wave source. *Pure and Applied Geophysics*, **150**, 661–676. 3, 6, 7

SOMA, H., NIITSUMA, H. & BARIA, R. (2002a). Reflection technique in time-frequency domain using multicomponent acoustic emission signals and application to geothermal reservoirs. *Geophysics*, **67**, 928–938, doi:10.1190/1.1484535. 7, 58

SOMA, N. & NIITSUMA, H. (1997). Identification of structures within the deep geothermal reservoir of the kakkonda field, japan, by a reflection method using acoustic emission as a wave source. *Geothermics*, **26**, 43–64. 6, 7

SOMA, N., NIITSUMA, H. & BARIA, R. (2002b). Deep sub-vertical structure at Soultz Hot Dry Rock site estimated by reflection technique using multicomponent acoustic emission events. *Trans. Geotherm. Resour. Counc.*, **26**, 255–266. 8

SOMA, N., NIITSUMA, H. & BARIA, R. (2007). Reflection imaging of deep reservoir structure based on three-dimensional hodogram analysis of mumicroseismic waveforms. *J. Geophys. Res.*, **112**, B1103, doi:10.1029/2005JB004216. 3, 7, 9, 23

TAKAHASHI, T. (1995). Prestack migration using arrival angle information. *Geophysics*, **60**, 154–163. 20

TAMAKAWA, K., ASANUMA, H., NIITSUMA, H. & SOMA, N. (2010). Principles of a seismic reflection method using AE multiplets as a source. In *Renewable Eenergy 2010 Proceedings*. 7, 58

TEANBY, N., KENDALL, J.M., JONES, R. & BARKVED, O. (2004). Stress-induced temporal variations in seismic anisotropy observed in microseismic data. *Geophysical Journal International*, **156**, 459–466. 2

THURBER, C., ROECKER, S., ZHANG, H., BAHER, S. & ELLSWORTH, W. (2004). Finescale structure of the san andreas fault zone and location of the safod target earthquakes. *Geophysical Research letters*, **31**, doi:10.1029/2003GL019398. 32, 38

TOPPOZADA, T., BRANUM, D., REICHLE, M. & HALLSTROM, C. (2002). San Andreas fault zone, California: M 5.5 earthquake history. *Bulletin of the Seismological Society of America*, **92**, 2555–2601. 28

VALLEY, B. & EVANS, K.F. (2006). Stress orientation at the Basel geothermal site from wellbore failure analysis in BS1. Tech. Rep. ETH 3465/56, ETH Zürich. 68

VALLEY, B. & EVANS, K.F. (2009). Stress orientation to 5km depth in the basement below Basel (Switzerland) from borehole failure analysis. *Swiss Journal of Geosciences*, **102**, 467–480. 89, 90, 91

WALDHAUSER, F. (2001). HypoDD: A computer program to compute double-difference hypocenter locations. Report, U.S. Geol. Surv. Open File Rep., 01-113. 47

WALDHAUSER, F. & ELLSWORTH, W. (2000). A double-difference earthquake location algorithm: Method and application to the northern Hayward fault, California. *Bulletin of the Seismological Society of America*, **90**, 1353–1368. 47

ZHANG, H., WANG, P., VAN DER HILST, R., TOKSOZ, M., THURBER, C. & ZHU, L. (2009). Three-dimensional passive seismic waveform imaging around the safod site, california, using the generalized radon transform. *Geophysical Research Letters*, **36**, L23308. 27, 28

ZOBACK, M. & HARJES, H.P. (1997). Injection induced earthquakes and the crustal stress at 9 km depth at the ktb deep drilling site. *Journal of Geophysical Research*, **102**, 477–492. 44

ZOBACK, M., HICKMAN, S. & ELLSWORTH, W. (2010). Scientific Drilling Into the San Andreas Fault Zone. *Eos, Transactions American Geophysical Union*, **91**, 197–199. 29, 39

List of publications

2013   A. Reshetnikov, J. Kummerow, S. A. Shapiro, H. Asanuma, and M. Häring. 2013. Microseismic Reflection Imaging of Basel EGS stimulated reservoir. Geophysics. Article in preparation.

A. Reshetnikov, J. Kummerow, S. A. Shapiro, H. Asanuma, and M. Häring. 2013. Microseismic Reflection Imaging of Stimulated Reservoirs and Fracture Zones. 75th EAGE Conference & Exhibition-Workshops.

C. Schmelzbach, J. Kummerow, P. Wigger, A. Reshetnikov, and S.A. Shapiro. 2013. Seismic-reflection imaging of the crust using earthquake waveform recordings-A case study from the Central Andes. EGU General Assembly Conference Abstracts (Vol. 15, p. 13862).

2012   A. Reshetnikov, J. Kummerow, S. A. Shapiro, H. Asanuma, and M. Häring. 2012. Microseismic reflection imaging using data from a hydraulic reservoir stimulation. 2012 Fall Meeting, AGU, San Francisco, USA.

J. Kummerow, A. Reshetnikov, M. Hring, and H Asanuma. 2012. 3-D Vp/Vs Ratio Distribution in the Geothermal Reservoir at Basel, Switzerland, from Microseismic Data. 2012 Fall Meeting, AGU, San Francisco, USA.

A. Reshetnikov, J. Kummerow, S. A. Shapiro, H. Asanuma, and M. Häring. 2012. Multi-source multi-receiver microseismic reflection imaging: Case study Basel. SEG Technical Program Expanded Abstracts 2012.

J. Kummerow, A. Reshetnikov, M. Hring, and H Asanuma. 2012. Distribution of the Vp/Vs Ratio within the Basel 1 Geothermal Reservoir from Microseismic Data. EAGE Conference & Exhibition: extended abstract, Copenhagen, Denmark.

2011   A. Reshetnikov, J. Kummerow, S. A. Shapiro, H. Asanuma, and M. Häring. 2011. Using Microseismicity to Image the Structure of the Basel Geothermal Reservoir. 73rd EAGE Conference & Exhibition: extended abstract. Vienna, Austria.

J. Kummerow, A. Reshetnikov, S. A. Shapiro, H. Asanuma, and M. Hring. 2011. Application of a Waveform Similarity- Based Location Algorithm to the Basel 1 Microseismic Data. European Geosciences Union General Assembly 2011. Vienna, Austria.

A. Reshetnikov, M. Jaya, S. Buske, J. Kummerow, and S. A. Shapiro. 2011. Characterisation of a geothermal reservoir using microseismic data. European Geosciences Union General Assembly 2011. Vienna, Austria.

A. Reshetnikov, J. Kummerow, S. Buske and S. A. Shapiro. Microseismic imaging at KTB. 2011. 71st DGG Annual meeting. Cologne, Germany.

2010   A. Reshetnikov, S. Buske, and S. A. Shapiro. Seismic imaging using microseismic events: Results from the San Andreas Fault System at SAFOD. 2010. Journal of Geophysical Research, 115, B12324, doi:10.1029/2009JB007049.

2010 A. Reshetnikov, J. Kummerow, S. Buske, S. A. Shapiro. 2010. Microseismic imaging from a single geophone: KTB. SEG Expanded Abstracts 29, 2070, Denver, USA.

A. Reshetnikov, J. Kummerow, S. Buske, S. A. Shapiro. 2010. Microseismic Imaging at KTB. 72nd EAGE Conference & Exhibition: extended abstract, Barcelona, Spain.

M. S. Jaya, S. Buske, J. Kummerow, A. Reshetnikov, S. A. Shapiro. 2010. Seismic Attribute Analysis of the 3-D Depth Migrated Image and Its Correlation with the Induced Microseismicity. Proceedings World Geothermal Congress 2010, Bali, Indonesia.

2009 A. Reshetnikov, S. Buske, S. A. Shapiro. Active Seismic Imaging Using Microseismic Events: Results From the San Andreas Fault System at SAFOD. 2009. AGU Fall Meeting: expanded abstracts, San Francisco, USA.

A. Reshetnikov, S. Buske, S. A. Shapiro. Active Seismic Imaging Using Microseismic Events. 2009. SEG Expanded Abstracts 28, 1668, Houston, USA.

A. Reshetnikov, S. Buske, S. A. Shapiro. Active Seismic Imaging Using Microseismic Events. 2009. 71st EAGE Conference & Exhibition: extended abstract, Amsterdam, Netherlands.

M.S. Jaya, S. Buske, J. Kummerow, A. Reshetnikov, S.A. Shapiro. 2009. Seismic Attribute Analysis of the 3-D Depth-migrated Image and Its Correlation With the Induced Microseismicity. 71st EAGE Conference & Exhibition: extended abstract, Amsterdam, Netherlands.

S. Buske, S. Gutjahr, A. Reshetnikov, S. A. Shapiro. 2009. Seismic imaging of the San-Andreas-Fault system at SAFOD. EGU General Assembly, Viena, Austria.

A. Reshetnikov, S. Buske, S. A. Shapiro. 2009. Active seismic imaging using microseismic events. EGU General Assembly, Viena, Austria.

2008 A. Reshetnikov, S. Buske, S. A. Shapiro. Active seismic imaging using microseismic events: results from the San-Andreas-Fault system at SAFOD. 2008. AGU Fall Meeting: expanded abstracts, San Francisco, USA.

S. Gutjahr, S. Buske, A. Reshetnikov, S. A. Shapiro. 2008. New Seismic Images of the San-Andreas-Fault System at SAFOD. AGU Fall Meeting: expanded abstracts, San Francisco, USA.

2007 A. Mukhin, A. Reshetnikov, I. Girman. 2007. Technology of direct and single-reflected elastic waves field calculation for 3D non-parallel layered models. 6th Conference and Exhibition Galperin Readings, Moscow, Abstract. (published in Russian)

U. Stepchenkov, A. Reshetnikov, I. Girman. 2007. Velocity model parameters estimation from walkaway and 3D VSP data. 6th Conference and Exhibition Galperin Readings, Moscow, Abstracts. (published in Russian)

2006 A. Reshetnikov, A. Mukhin, A. Tabakov, V. Eliseev, 2006. Technology and application results of the dynamic decomposition and reconstruction of wavefields (DDR) for synthetic data. Seismic Technology. 2. p. 14-18. (published in Russian)

114

2006 U. Stepchenkov, A. Tabakov, A. Reshetnikov, N. Rykovskaya, K. Baranov. 2006. Velocity model buidling using full VSP wavefield. Seismic Technology. 2. (published in Russian)

A. Reshetnikov, A. Tabakov, A. Mukhin, I. Girman. 2006. Technology of calculation of elastic waves kinematic characteristics using ray-tracing method in the case of multiple ray paths. 6th Conference and Exhibition Galperin Readings, Moscow, Abstracts. (published in Russian)

U. Stepchenkov, A. Reshetnikov, A. Tabakov, A.Kolosov. 2006. Generation of velocity model using multiple waves from several VSP sources. 6th Conference and Exhibition Galperin Readings, Moscow, Abstracts. (published in Russian)

2005 A. Reshetnikov, A. Mukhin, A. Tabakov, V. Eliseev, 2005. DDR: the technology and results of synthetic and real data processing. 5th Conference and Exhibition Galperin Readings, Moscow, Astracts. 40-44. (published in Russian)

U. Stepchenkov, A. Tabakov, A. Reshetnikov, 2005. Estimation of the velocity model from full vector VSP wave field. 5th Conference and Exhibition Galperin Readings, Moscow, Abstracts. 31-35. (published in Russian)

2004 A. Reshetnikov, V. Reshetnikov, A. Tabakov, V. Eliseev. 2004. Ray method for the problem of dynamic decomposition of wave fields and reconstructing the model for VSP data . Seismic Technology. 1. p. 66-70. (published in Russian)

A. Reshetnikov, U. Stepchenkov, A. Tabakov, V. Eliseev. 2004. Joint imaging of the media using different wave types. 4th Conference and Exhibition Galperin Readings, Moscow, Abstracts. 60-62. (published in Russian)

A. Reshetnikov, U. Stepchenkov, A. Tabakov, V. Eliseev. 2004. Raytracing of 3d models with velocity gradients. 4th Conference and Exhibition Galperin Readings, Moscow, Abstracts. (published in Russian)

2003 A. Reshetnikov, V. Reshetnikov, I. Soltan, A. Tabakov. 2003. Dynamic decomposition of seismic wavefields and media model reconstruction with raytracing method by VSP data. International Conference and Exhibition Geophysics of the XXI Century – Leap into the Future, Moscow, Expanded Abstracts.

2002 A. Tabakov, I. Soltan, A. Reshetnikov, V. Reshetnikov. 2002. Dynamic decomposition of the wavefield and reconstruction of the media in VSP data processing. 2nd Conference and Exhibition Galperin Readings, Moscow, Abstracts. 12-13. (published in Russian)